



Review

A review on current anode materials for rechargeable Mg batteries

Dajian Li^{a,*}, Yuan Yuan^{b,*}, Jiawei Liu^b, Maximilian Fichtner^{c,d}, Fusheng Pan^b^a Karlsruhe Institute of Technology, Institute for Applied Materials-Applied Materials Physics (IAM-AWP), Hermann-von-Helmholtz-Platz 1, 76344 Eggenstein-Leopoldshafen, Germany^b National Engineering Research Center for Magnesium Alloys (CCMG), College of Materials Science and Engineering, Chongqing University, 400044 Chongqing, China^c Karlsruhe Institute of Technology, Institute of Nanotechnology (INT), Hermann-von-Helmholtz-Platz 1, 76344 Eggenstein-Leopoldshafen, Germany^d Helmholtz-Institute Ulm (HIU), Helmholtzstr. 11, 89081 Ulm, Germany

Received 2 May 2020; received in revised form 19 September 2020; accepted 29 September 2020

Available online xxx

Abstract

There is an increasing demand for rechargeable batteries in high-performance energy storage systems. The current dominating Li-ion batteries are limited by price, resource availability, as well as their theoretical capacities. So that the community has started to explore alternative battery chemistries. As a promising multivalent battery type, rechargeable magnesium batteries (RMBs) have attracted increasing attention because of high safety, high volumetric energy density, and low cost thanks to abundant resource of Mg. However, the development of high-performance anodes is still hampered by formation of passivating layers on the Mg surface. Additionally, dendrites can also grow under certain conditions with pure Mg anodes, which requires further studies for reliable operation window and substitutes. Therefore, this review specifically aims to provide an overview on the often overlooked yet very important anode materials of RMBs, with the hope to inspire more attention and research efforts for the achievement of over-all better performance of future RMBs.

© 2020 Published by Elsevier B.V. on behalf of Chongqing University.

This is an open access article under the CC BY-NC-ND license (<http://creativecommons.org/licenses/by-nc-nd/4.0/>)

Peer review under responsibility of Chongqing University

Keywords: Rechargeable Mg batteries; Anode materials.**1. Introduction**

Since the invention of lead-acid battery in the year 1859, rechargeable batteries have become an indispensable part for modern society, especially for the portable applications. Up to today, lithium-ion batteries (LIBs) are the most successful rechargeable battery system because of their high energy and power density compared to nickel–cadmium (NiCd) or nickel–metal hydride (NiMH) batteries [1,2].

Although LIBs have achieved great success, people are continuously looking for novel batteries to achieve higher safety, energy and power density [3]. Especially, the energy capacity of LIBs is still unsatisfactory. Currently, the charge capacity of LIBs is restricted by the cathode materials, which

can be mostly classified into three types according to their crystal structures as layered structure (LiCoO_2 , theoretical capacity 274 mA h g^{-1}), spinel structure (LiMn_2O_4 , theoretical capacity 148 mA h g^{-1}), and olivine structured polyanionic compounds (LiFePO_4 , theoretical capacity 170 mA h g^{-1}) [4]. Due to limited potential lattice positions of removable Li ions in certain crystal structures, further increase of charge capacity of LIBs can be quite difficult.

Beside capacity limitation, emerging large-scale applications instead of portable electronics demand higher quantity of materials supply, and forces scientific and industrial societies [5,6] to look for more abundant alternatives compared to Li [7]. Recently, sodium-ion batteries (SIBs) have stimulated extensive studies due to the natural abundance of Na and no need for expensive Cu and Co in the SIB [8]. However, while the expected price of SIB is lower than that of LIB, SIBs have intrinsic low energy densities compare to LIBs. The operation

* Corresponding authors.

E-mail addresses: dajian.li@kit.edu, lidajian@gmail.com (D. Li), yuanyuan17@cqu.edu.cn (Y. Yuan).

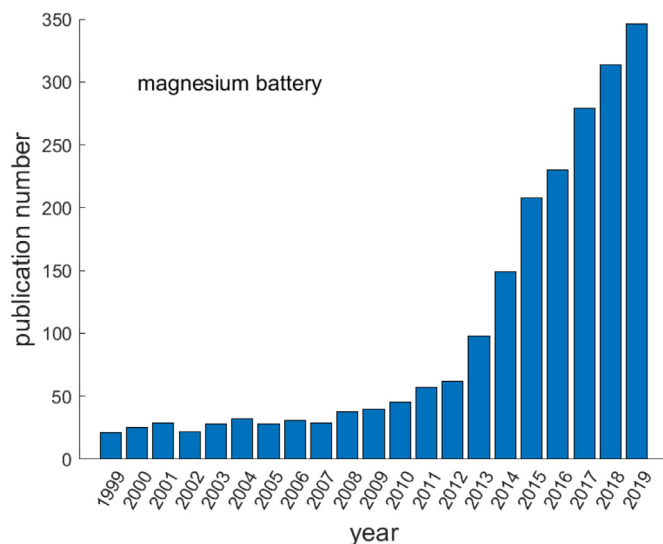


Fig. 1. publication number with topic of “magnesium battery” in web of science between the years 1999 and 2019.

voltages of SIBs are approximately 0.3 V lower than that of LIBs, which means energy density is also limited. The first commercial 18650 SIBs launched by CNRS and RS2E can provide 2000 cycles but only at 90 W h kg^{-1} [9], while the LIB has reached 240 W h kg^{-1} at cell level [5].

In order to develop systems with high gravimetric and volumetric energy densities, as well as improved safety, power density, lifetime, and reduced cost, intercalation batteries based multivalent (MV) chemistries such as Mg^{2+} , Ca^{2+} , Zn^{2+} , Al^{3+} , etc., have attracted growing interest in the last decade [10].

Among the MV intercalation batteries, rechargeable magnesium batteries (RMBs) have attracted numerous attentions because Mg metal can provide high capacity (volumetric capacity, $E_{V,\text{Mg}}=3833 \text{ mA h cm}^{-3}$), low reduction potential (-2.4 V vs. SHE) and dendrite-free deposition with up to 100% coulombic efficiency in the cells under certain operation conditions [11,12]. Additionally, Mg is the 8th abundant element in the earth’s crust, and resource limitations are not in sight [13,14]. Fig. 1 shows number of publications with the topic of “magnesium battery” on web of science for two decades up to year 2019.

RMB has long been considered as a promising energy storage technique, but there have been delays in the development for several reasons. First developments of [13,15] have allowed fast charge RMBs with working potential window up to 2.1 V vs. Mg. A persisting challenge is the diffusion of Mg^{2+} , which is sluggish in the cathode part, this will cause voltage hysteresis and insufficient magnesiation degree during cell operation. Due to the urgency for high performance cathodes for RMBs, most publications focus on this area [11,16–18].

Beside cathodes, proper electrolytes are also widely considered as the bottleneck for development of high-performance RMBs. A comprehensive review for the development of electrolytes and their compatibility with an-

ode materials has been given in [19]. Although the organohaloaluminate-based electrolytes can prevent passive layer formation on the Mg metal surface and have delighted the hope of pure Mg metal anode for RMBs [13], they are not stable for the high voltage cathodes and limited theoretical energy capacity. Recent developed electrolytes enable fast and reversible stripping and plating with high efficiencies in voltage windows $> 4\text{ V}$ [20], and with no detrimental release of halide ions, which would corrode parts of the cell [21,22].

In many review papers, the anode side of RMBs is neglected, with only one statement as Mg anode is dendrite-free deposition with up to 100% coulombic efficiency [23]. However, Whittingham and Banerjee have recently stressed that the safety of using Mg metal cannot be fully guaranteed as they are not totally free of dendrite formation [24]. Additionally, incompatibility between Mg metal and conventional electrolytes has long been the major obstacle for the development of RMBs because Mg strongly tend to form passivating surface films with many solvents and subsequently block further electrochemical reactions. Regardless numerous efforts have been dedicated to the study of cathodes and electrolytes, no satisfactory battery performance together with pure Mg anode has been developed for RMBs up to now. Therefore, the development of alternative anode materials is still necessary to expand the potential candidates of suitable electrolytes and cathodes. We have to bear in mind that the compatibility between anodes, cathodes, electrolytes, as well as other battery components, such as separators and shells, must be fulfilled during development of novel RMBs. A compilation of reviews of Mg anode has been given in [25]. During the preparation of the current manuscript, Niu, Zhang and Arubach has made a review for the alloy anode materials for RMBs based on groups IIIA, IVA, VA elements [26]. Nevertheless, the current review aims to include the latest updates and further bring attention to the importance of anode side of RMBs, their existing problem, and encourage the efforts to overcome them.

2. Pure Mg as anode

Mg was initially considered to be dendrite free when applied as anode of secondary batteries. However, this conclusion is highly dependent on the electrolyte and current density [27]. Recent studies showed that some applications under fast charge or low-temperature conditions may cause severer dendrite growth than that Li anodes for LIBs [24,28]. Additionally, interferences of pure Mg anodes and electrolytes can be problematic due to high polarizing ability of Mg^{2+} cations. Lu et al. [29] found passive films, which can impede or block Mg ions in their migration towards the electrode surface. In fact, bulk Mg anode is not a functional reversible electrode in some polar organic electrolytes due to the formation of passivating barriers [30]. Therefore, a series of efforts have been dedicated to the improvement not only of Mg electrolytes, but also of Mg anodes and their compatibility with the electrolyte.

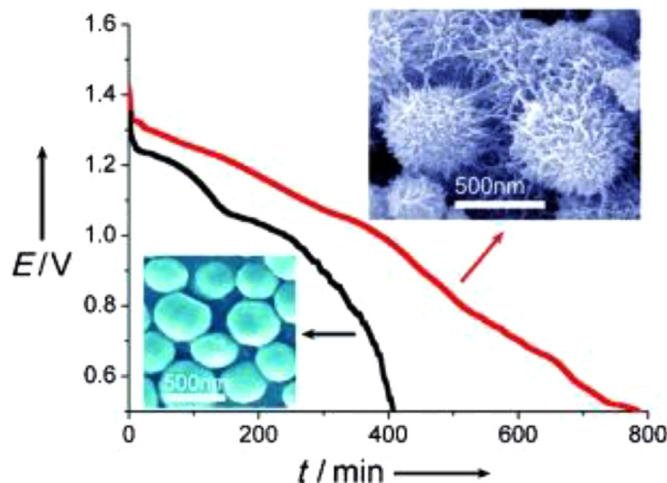


Fig. 2. Representative discharge curves of the Mg/air batteries made from Mg particles with different morphologies, at a constant current of 0.5 mA and a temperature of 25°C [36] (reproduced with permission).

Recently, Son et al. [31] prepared slurry by mixing Mg powder with carbon black, polyacrylonitrile (PAN) and $Mg(CF_2SO_3)_2$ in dimethylformamide (DMF). The coated electrolyte was subsequently annealed at 300°C for 1 h under Ar to obtain an artificial interphase on the Mg metal. The coated Mg electrode showed similar deposition/stripping behaviour to that of pristine Mg electrode in APC electrolyte but over 1000 cycles in PC-based electrolyte solution, which can form impermeable passivation film with bare Mg. Full cell assembled using coated Mg anode and V_2O_5 cathode, exhibited reversible capacities of 47 mA h g^{-1} and 140 mA h g^{-1} with PC and PC+3 M H_2O electrolytes, respectively [31]. However, Attias et al. [19] questioned if the insertion process with V_2O_5 cathode was actually related to protons instead of Mg ions.

Lv et al. [32] used $SnCl_2$ -DEM solution to treat Mg foils and get an Sn-based artificial layer, which exhibited a long lifespan (over 4000 cycles, 1400 h) in the subsequent stripping/plating measurements at current density of 6 mA cm^{-2} . Zhang et al. [33] added $GeCl_4$ into $Mg(TFSI)/DME$ electrolyte and allowed ion exchange of $Ge^{4+} + Mg \rightarrow Ge + Mg^{2+}$ inside assembled cell to form a Ge based artificial layer, which showed a self-repair process in engraving-reassembling experiment. Full cells using Mg coupled with Ti_2S_2 or Ti_3C_2 in the modified electrolyte both delivered revisable capacity around 80 mA h g^{-1} after 40 cycles.

Due to increased specific surface areas, nanomerization can make Mg more reactive [34,35]. Li et al. [36] prepared controlled nano/mesostructures with spherical, platelike, rodlike, and sea-urchin-like shapes using a vapour-transport approach. Fig. 2 shows the discharge curves of Mg-air battery using spherical and sea-urchin-like shape Mg particles with similar diameters. Higher discharge voltage, longer discharge time and higher energy density has been obtained using the sea-urchin-like shape Mg particles.

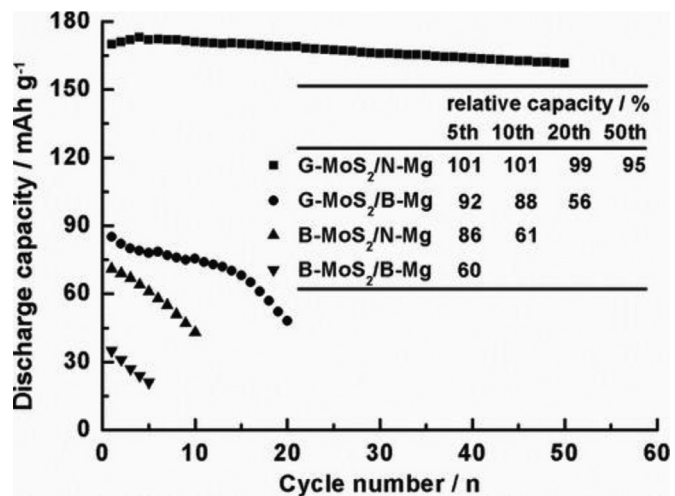


Fig. 3. Cell behaviours bulk (B) or graphene-like (G) MoS_2 cathode and bulk (B) or nanosize (N) Mg anode with a discharge rate of 20 mA g^{-1} [30] (reproduced with permission).

Liang et al. [30] prepared ultrasmall Mg nanoparticles (mostly below 3 nm diameter), combined with graphene-like MoS_2 as cathode material. The cyclability of constructed RMBs was significantly improved compared to bulk-Mg anode, as shown in Fig. 3. Liang et al. also proposed that the improved performance of nanostructured Mg anode can be attributed to increased surface area, which can lead to thinner passivating film and improved kinetic of Mg ion migration during cell operation.

3. Metallic anode

3.1. Group XIV elements (Si, Ge, Sn, and Pb)

Several types of metallic anodes have been developed for applications of RMBs. Inspired by the application to LIBs, the group XIV metallic elements, i.e. Si, Ge, Sn, and Pb, have been studied for their suitability as anode materials for RMBs.

Si, Ge, and Sn share the same diamond structure (α), which can host up to 2 moles of Mg atoms with two kinds of possible lattice sites for 1 mole anode material, as shown in Fig. 4. When combined with Mg element, Si, Ge and Sn also share very similar phase diagrams, which shows only one intermetallic compound, Mg_2X (X=Si [37], Ge [38], Sn [39]), and negligible solubility at both sides of each phase diagram.

If the reaction between Mg and Si, Ge, or Sn follows the corresponding equilibrium phase diagram, only one voltage plateau should appear during each battery application [41]. However, Wang et al. [42] found that Si, Ge and Sn can become amorphous during magnesiation process. The predicated [42] multi voltage plateaus for magnesiation of amorphous Si, Ge, and Sn are shown in Fig. 5. According to Wang et al. [42], Mg diffusivity in Si ($\sim 10^{-17} \text{ cm}^2/\text{s}$) is much lower than that in Ge and in Sn ($\sim 10^{-14}$ to $10^{-13} \text{ cm}^2/\text{s}$). Additionally, crystalline Si and Ge are not practical due to the required

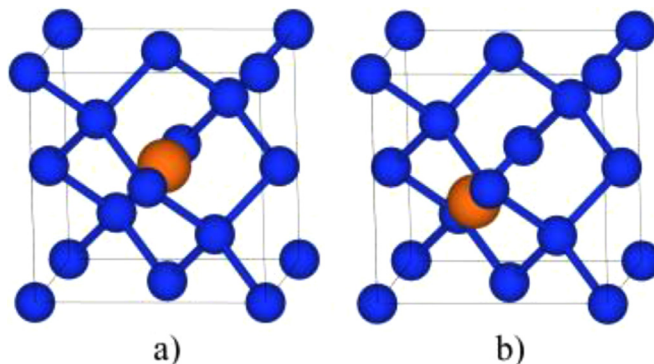


Fig. 4. Tetragonal (a) and hexagonal (b) insertion sites for Mg (orange) in Ge, Si, and Sn (blue) [40] (reproduced with permission).

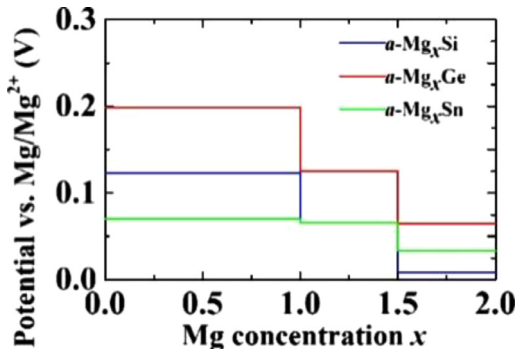


Fig. 5. Electrode potentials vs Mg/Mg^{2+} for amorphous (a-) Mg_xX ($\text{X} = \text{Si}$, Ge, and Sn) as a function of Mg concentration x predicated using ab initio calculation [42] (reproduced with permission).

high overpotential. Therefore, regardless the highest theoretical capacity of Si (3817 mA h g^{-1}) [40], most studies focused on Sn (theoretical capacity 911 mA h g^{-1}) anode application.

Besides diamond structure, Sn also can crystallize into tetragonal structure ($\beta - \text{Sn}$). But the formation of $\beta - \text{Sn}$ leads to higher Mg diffusion barriers (0.435 eV) compare to that with $\alpha - \text{Sn}$ (0.395 eV) [43]. Moreover, an already existing Mg ion near the diffusing Mg ion will increase its diffusion barrier to 0.77 eV for the $\beta - \text{Sn}$ [44]. Therefore, $\beta - \text{Sn}$ is not a suitable candidate for RMB applications. Jin and Wang [45,46] calculated the Mg diffusion behaviour through different crystal faces in $\alpha - \text{Sn}$ using DFT, and found the lowest diffusion energy barrier for Mg along the $\langle 100 \rangle$ direction.

Singh et al. [47] obtained a discharge capacity up to 903 mA h g^{-1} for the first cycle using Sn electrode against pure Mg, as shown in Fig. 6. The measured insertion/extraction voltage were 0.15/0.2 V against pure Mg under 0.002 C current rate. The formation/decomposition of the Mg_2Sn phase was simultaneously confirmed using XRD technique.

Although Singh et al. [47] obtained near theoretical discharge capacity using Sn electrode for the first discharge process, only about 1/3 of the capacity was recovered during the following charge process. Nguyen et al. [48] assembled half cells using Sn powder electrode and obtained a reversible capacity up to 334 mA h g^{-1} , which is comparable to the re-

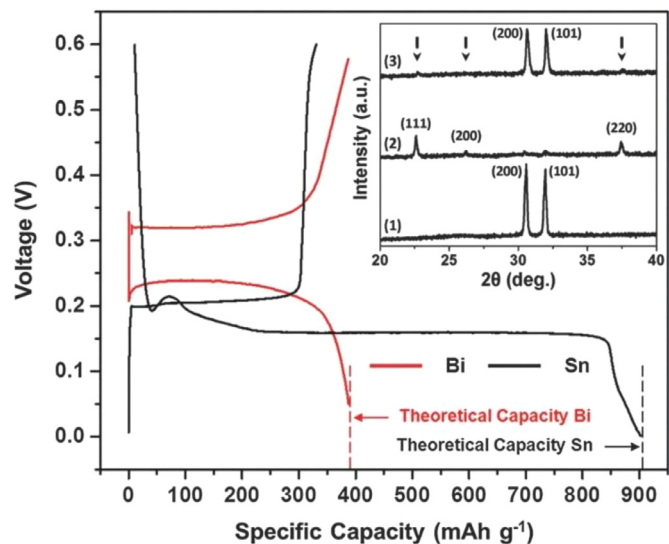


Fig. 6. 1st cycle galvanostatic magnesiation/de-magnesiation curves for Sn/Mg and Bi/Mg half-cells. Inset – XRD spectra for (1) as-fabricated, (2) magnesiated and (3) demagnesiated Sn anode (peak positions marked for Mg_2Sn phase) [47] (reproduced with permission).

sults of Singh et al. [47]. Nguyen et al. [48] also prepared 49 nm thick Sn film to perform electrochemical test. After 50 cycles, 76% discharge capacity was retained with the Sn film, which also exhibited particle cracking and amorphization. Nacimiento et al. [49] used micro- and nano-particulate $\beta - \text{Sn}$ to assemble RMBs. Within half-cell setup, the microparticulate Sn exhibited low specific capacity less than 10 mA h g^{-1} . The nanoparticulate Sn delivered initial capacity of 225 mA h g^{-1} , but also fast capacity to less than 50 after 50 cycles at 0.05 C current. However, nanoparticulate Sn showed specific capacity up to 150 mA h g^{-1} when combined MgMn_2O_4 cathode [49].

Because most state-of-art RMB cathodes are Mg free compounds [16,23], anodes often serve as the Mg sources in RMBs. Nguyen and Song [50,51] synthesised Mg_2Sn phase alloy using ball-milling technique starting from pure Mg and Sn powder. The obtained Mg_2Sn phase was combined with V_2O_5 cathode to obtain full cells, which exhibited good electrochemical performance [50], as shown in Fig. 7. Asl et al. [52] also prepared Mg_2Sn phase by melting weighted Mg and Sn. The obtained ingot was subsequently crushed, powdered and ball-milled using high-energy mill. The obtained micrometer-sized Mg_2Sn phase crushed into nano sized Sn particles during the initial magnesiation/demagnesiation cycles, which resulted better performance for the cycles afterwards.

Parent et al. [53] used nanosized β -SnSb particles as starting material and found that after several charge-discharge cycles, the particles irreversibly transform into Sn and Sb-rich subparticles. In the following cycles, Sn-rich subparticles show highly reversible Mg-storage while Sb-rich subparticles contribute little to the performance. Therefore, Parent et al. [53] stated that good cyclability can be expected in RMBs only if the particle size of Sn anode is smaller than 40 nm in diameter.

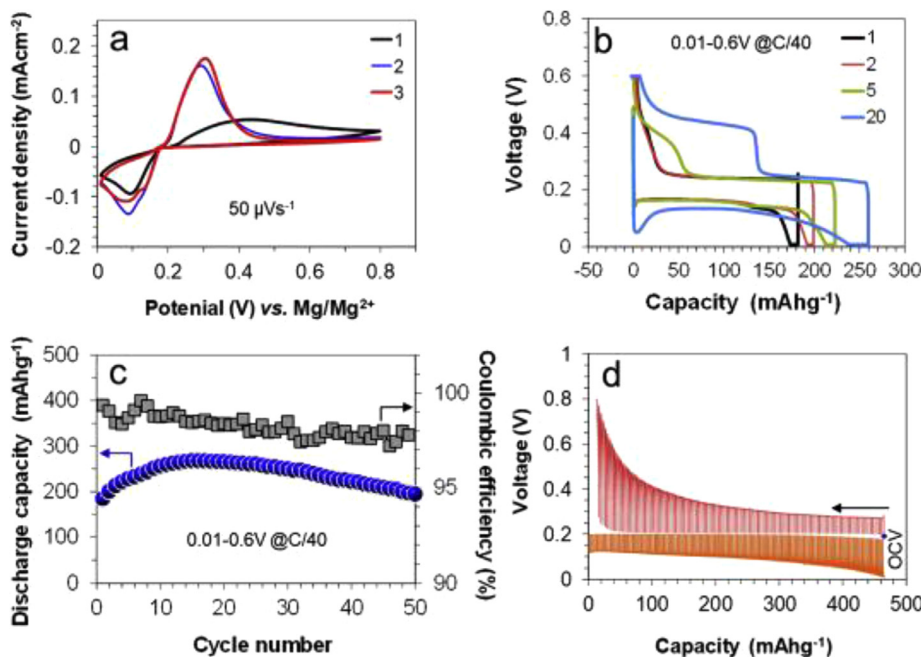


Fig. 7. Electrochemical characteristics of Mg_2Sn anode. (a) Cyclic voltammogram at the scan rate of 50 mV s^{-1} ; (b) Discharge-charge voltage profiles; (c) cycling performance;(d) GITT curves [50] (reproduced with permission).

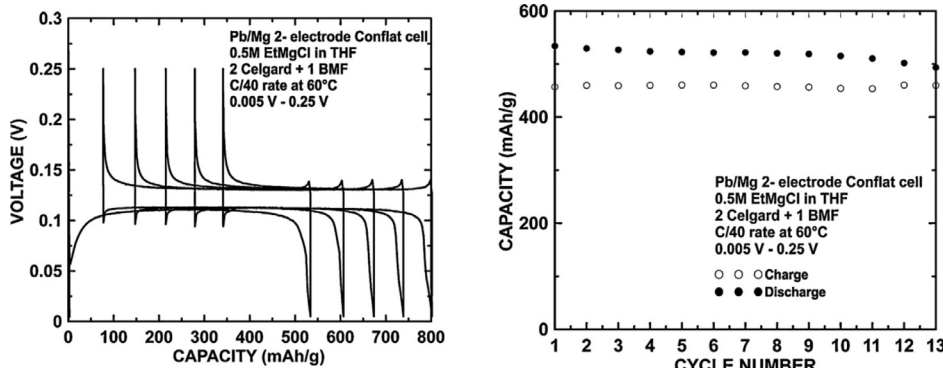


Fig. 8. Cell performance of a sputtered Pb film electrode vs. Mg [54]. (a) Voltage curve; (b) Cycling performance (reproduced with permission).

Periyapperuma et al. [54] investigated magnesiation of Pb in film and powder form. The Pb film was sputtered on stainless steel foil with an average thickness of $0.24\text{ }\mu\text{m}$. A reversible capacity about 450 mA h g^{-1} (see Fig. 8) was obtained using ethylmagnesium chloride electrolyte and Mg foil counter electrode. Periyapperuma et al. [54] also built similar batteries using Pb powder (325 mesh), but only obtained about half of the reversible capacity compare to the ones using Pb foil. It should be noticed that the potential of Pb-Mg alloys is only about 125 mV against pure Mg, which is the lowest among known alloy anodes for RMBs. Therefore, it is possible to obtain higher voltage RMBs by using Pb as the anode material.

3.2. Bismuth

Besides Sn, Bi is also considered as the most promising alloy anode element for RMBs. Through the reaction

$3\text{Mg} + 2\text{Bi} \rightleftharpoons \text{Mg}_3\text{Bi}_2$, Bi can provide a theoretical specific capacity of 385 mA h g^{-1} . Although the specific capacity of Bi is not as high as Sn, theoretical volumetric capacity of Bi is 3783 mA h cm^{-3} , which makes it a promising anode candidate for RMBs. Additionally, Bi anodes also exhibited good kinetic performance and relative low reduction/oxidation potential for application of RMBs. Ab-initio calculations [44,46] showed that diffusion energy barrier of Mg in the $\text{Bi} + \text{Mg}_3\text{Bi}_2$ two-phase region locates in the range of 0.37-0.67 eV. However, Murgia et al. [55] reported that the two-phase region for $\text{Bi} + \text{Mg}_3\text{Bi}_2$ is characterized with an open-circuit voltage at 230 mV against pure Mg anode using GITT technique. Meanwhile, the diffusion barrier for Mg ions to move from the surface to subsurface sites was calculated to be 1.27 eV [46], which indicates that surface modification could be essential for improving the battery performance.

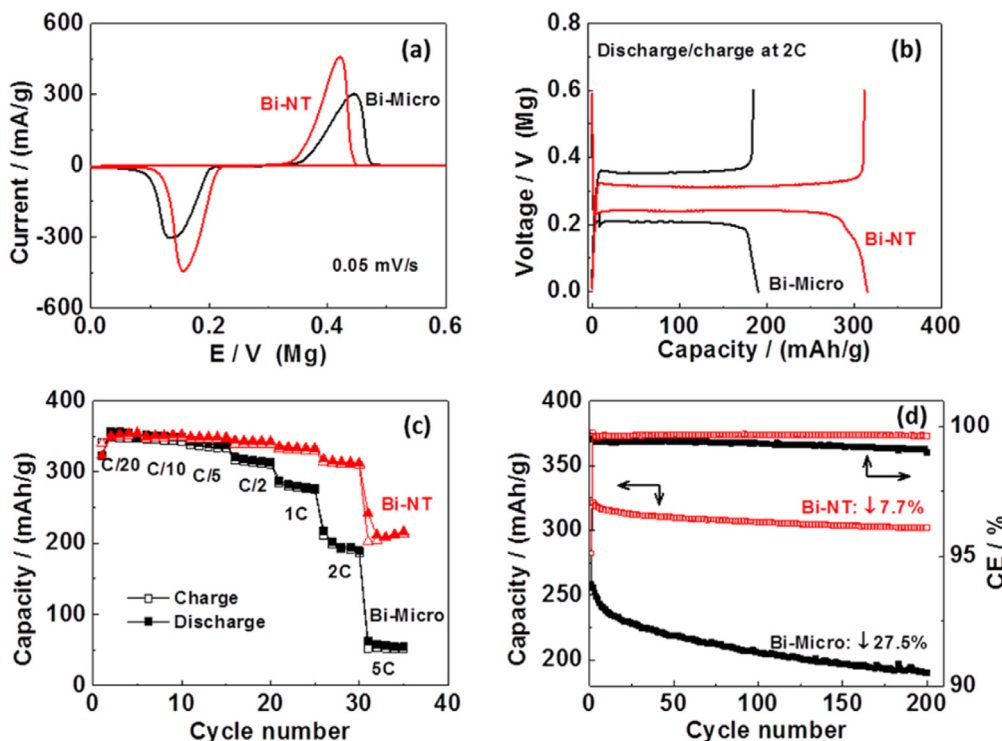


Fig. 9. Battery performances of Mg-Bi cells assembled with Bi nanotubes (NT) and microsized Bi powder [58]. (a) Cyclic voltammograms of magnesiation/demagnesiation; (b) discharge/charge profile; (c) rate performance; (d) cycling stability and Coulombic efficiency (reproduced with permission).

Many groups have assembled RMBs using pure Bi against Mg electrodes and demonstrated promising battery performances. Arthur et al. [56] applied Bi as the anode of RMBs and demonstrated a reversible capacity around 240 mA h g^{-1} , as shown in Fig. 9. DiLeo et al. [57] deposited Bi on C nanotubes and obtained a reversible capacity over 180 mA h g^{-1} . Shao et al. [58] used Bi nanotubes as anode for RMBs and obtained high reversible capacity of 350 mA h g^{-1} with a current at 0.05 C which is 91% of the theoretical capacity of pure Bi. After 200 cycles with 0.02 C current, the RMBs assembled with Bi nanotubes [58] still maintained 303 mA h g^{-1} reversible capacity. The excellent cell performance was attributed to the formation of even smaller nanoparticles from nanotubes during magnesiation/demagnesiation process. The newly formed nanoparticles remained connecting with each other to keep the charge capacities, while the formed nanopores served as fast ion transportation path.

Besides Shao et al. [58], several groups also reported that microstructures evolution of Bi electrode during operation of RMBs is essential for their performance. Murgia et al. [55] prepared half cells using micrometre particles of pure Bi and Mg_3Bi_2 . During rate-capacity tests, the batteries built using pure Bi powder [55] exhibited even higher capacity than that from Bi nanotubes [58]. Murgia et al. [55] confirmed the $\text{Bi} + \text{Mg}_3\text{Bi}_2$ biphasic mechanism using Operando XRD characterization, and considered that the electrochemical grinding process could act as an in situ self-nanostructuration for Bi electrodes in RMBs. Liu et al. [59] also found the capacity increase when using Bi nanowires as active material for

RMBs, and attributed the electrochemical grinding effect to the residual Mg_3Bi_2 phase. A clear nanostructuration of the Bi anodes has been reported by Ramanathan et al. [60] by using TEM to investigate the morphology evolution of Bi anode, as shown in Fig. 10. Benmayza et al. also investigated the thermal generation process for half cells with Bi anode during charge/discharge process, separated the total heat into irreversible and reversible part, plus the “other” part, which was attributed to pulverization/reformation of Bi material. A complex model to describe the porous electrode of Bi anode was later developed by the same group [61].

Although Bi anodes exhibit the self-nanostructuring property, electrodes prepared using nanosized Bi powder still exhibit better rate-capability as well as cycling stability in RMBs than that using bigger Bi particles, as shown in Fig. 11 [62]. Nevertheless, Kravchik et al. [62] observed that the Bi anode with 10 nm particles shows poorer capacity and cyclability than that with 18 nm ones, but did not give an explanation. Penki et al. [63] synthesized bismuth (Bi)/reduced graphene oxide (RGO) nanocomposites by using in situ reduction. The electrode made from composite of 60 % Bi and 40 % RGO delivered a specific discharge capacity of 413 mA h g^{-1} , which is even higher than the theoretical capacity of Mg_3Bi_2 (385 mA h g^{-1}), in the first cycle. It also retained 372 mA h g^{-1} in the 50th cycle. Penki et al. [63] attributed the good cyclability to RGO, which can minimize the mechanical stress during magnesiation/demagnesiation process. Wang et al. [64] prepared bismuth oxyfluoride (BiOF) using a solvothermal method. After the first discharge, during which

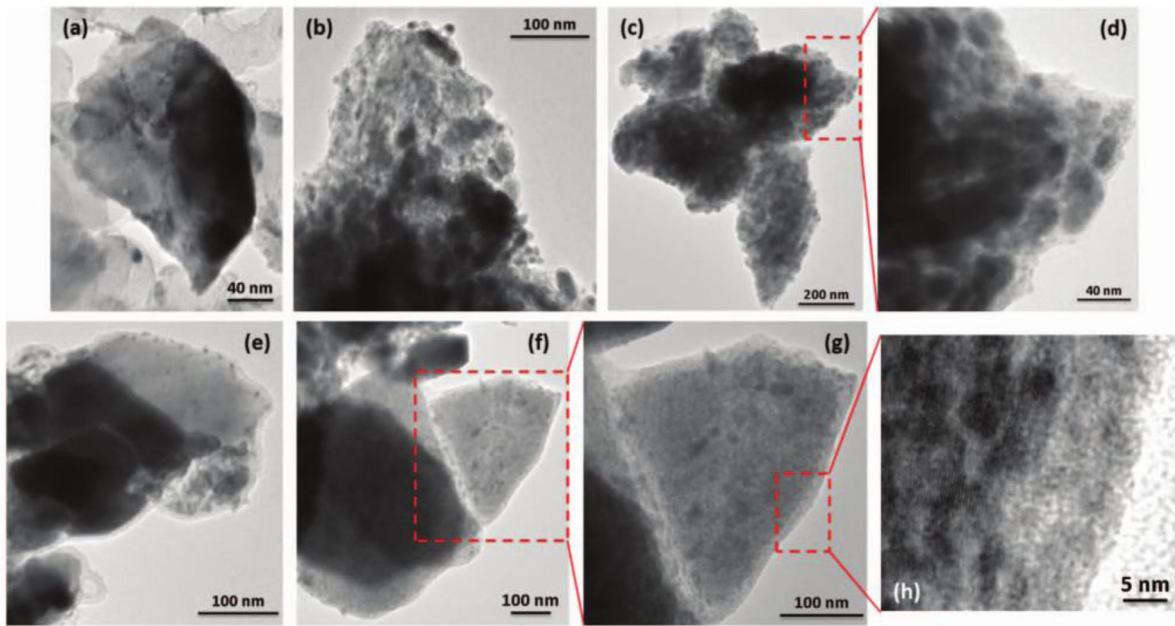


Fig. 10. TEM images depicting changes in the structure of Bi during the processes of magnesiation/demagnesiation, (a) pristine Bi, (b) 50% magnesiated Bi, (c) and (d) 100% magnesiated Bi (i.e. Mg_3Bi_2), (e) 50% demagnesiated Mg_3Bi_2 , (f) (g) and (h) 100% demagnesiated Mg_3Bi_2 (i.e. Bi) [60] (reproduced with permission).

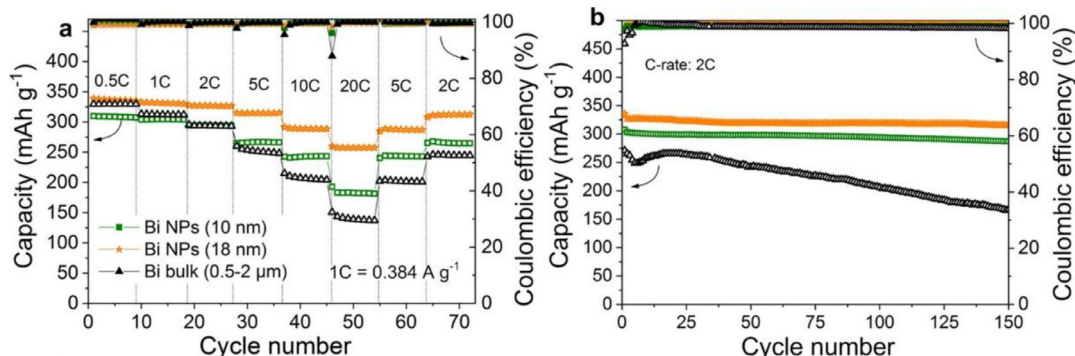


Fig. 11. (a) Rate-capability and (b) cycling stability measurements of Mg-ion half-cells using nano (10 and 18 nm, "NPs") and micro sized (0.5-2 μ m, "bulk") Bi anodes [62] (reproduced with permission).

metallic Bi was generated *in situ*, the BiOF delivered a reversible Mg storage capacity of 335 mA h g^{-1} and 273 mA h g^{-1} at 15 mA g^{-1} and 300 mA g^{-1} , respectively.

Due to the promising battery performance, attempts have been dedicated to reducing cost for large scale production of Bi anodes for RMBs. Tan et al. [65] sintered Mg_3Bi_2 alloys by heat treating Bi and Mg powders at 300, 500, 650 and 750°C. 650°C was found suitable for obtaining pure Mg_3Bi_2 phase alloy, which could deliver reversible capacity up to 350 mA h g^{-1} . Lower temperatures were found not sufficient for the reaction and diffusion, while 750°C caused too much Mg evaporation.

3.3. Antimony

Sb and Bi share many similarities, such as (1) both Sb and Bi are rhombohedral in crystal structure; (2) Sb and Bi

can form all proportional solid solution; and (3) both Sb-Mg or Bi-Mg phase diagrams contain similar intermetallic compounds (Mg_3Sb_2 and Mg_3Bi_2). Therefore, different groups also investigated Sb with the hope of finding another good anode candidate for RMBs with theoretical capacity of 660 mA h g^{-1} .

Arthur et al. [56] used Bi, Sb, and Bi-Sb alloys as RMB anodes to investigate their electrochemical performance. All alloys could get magnesiated (Fig. 12 (a)) and reach close to their theoretical capacities at 0.01 C current (Fig. 12 (b)). However, the pure Sb anode showed poor cyclability at 1 C rate while Bi-containing anodes still retain most of their magnesiation/demagnesiation capacities (Fig. 12 (c)). Parent et al. [53] found that the β -SnSb nanoparticles transformed into Sn and Sb-rich subparticles during the first several charge-discharge cycles. The Sn subparticles exhibit highly reversible Mg-storage. However, the Sb-rich subparticles showed little

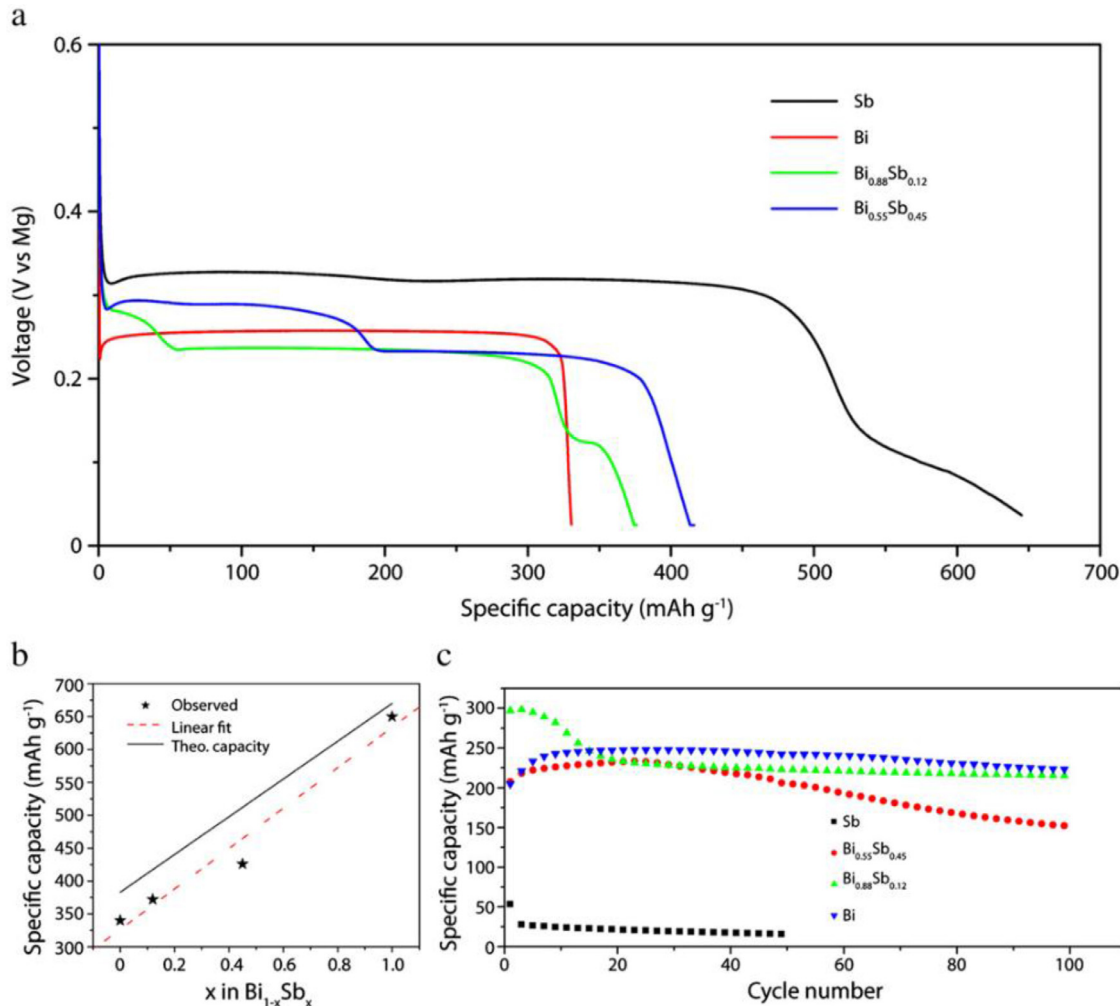


Fig. 12. (a) Galvanostatic discharge profile of Bi, Sb, $\text{Bi}_{0.88}\text{Sb}_{0.12}$ anodes at a 0.01 C rate. (b) Observed capacity of the alloy anodes with a linear fit of these capacities; dashed line compared with the theoretical capacity; solid line. (c) Cycling capabilities of Bi, Sb, $\text{Bi}_{0.88}\text{Sb}_{0.12}$ anodes at a 1 C rate [56] (reproduced with permission).

contribution to the charge-discharge capacity in the following cycles [53].

3.4. Others (In, Al, Li, Ga)

Murgia et al. [66] used micrometric In and MgIn powders as active material to study their battery performance against pure Mg. MgIn powders were prepared using high-energy ball milling technique; Mg-organohaloaluminate electrolyte was applied for the electrochemical investigations. Up to 425 mA h g⁻¹ revisable capacity was achieved at 0.02 C discharge rate for In powders. Good cyclability were also demonstrated with both In and MgIn initial active materials, as shown in Fig. 13. However, the battery performance decreased drastically with increasing current rate. Further investigations are required for the application of In anodes in RMBs.

Sivashanmugan et al. [67] used Mg-13Li alloy as anode material and declared that Mg-Li/MgCl₂/CuO cells could of-

fer higher operating voltages and capacities than Mg-Al alloys [68].

Wang et al. [69] took advantage of low melting point of Ga (27.6°C) and introduced liquid phase during RMB operation process. Coin cells with initial setup of $\text{Mg}_2\text{Ga}_5/\text{APC}+\text{LiCl}/\text{Mg}$ exhibited unprecedented long-cycle of 1000 cycles at high (dis)charge rate of 3 C at 40°C with a capacity above 200 mA h g⁻¹, and coulombic efficiency above 95%. The reversible reaction between liquid Ga and Mg at 40°C is given in Eq. (1). Coin cells with the same setup showed almost no cyclability at 20°C, which is below the melting point of Ga. Obviously, the presence of liquid Ga during battery operation was essential for the high-rate and long cycle-life RMB. Phase diagram of Ga-Mg system and schematic explanation of the self-healing mechanism is given in Fig. 14. In order to avoid all-solid reactions, the maximum Mg content in the Ga electrode was designed to not exceed Mg content of the Mg_2Ga_5 phase.



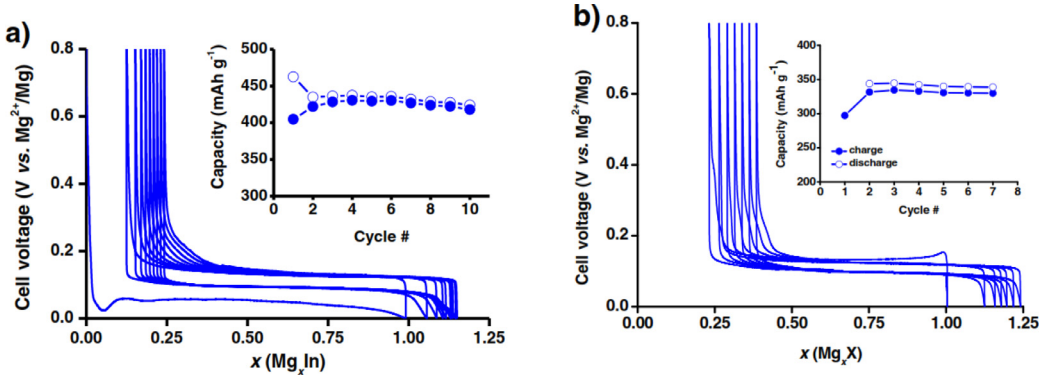


Fig. 13. Cycling performance with In/MgIn electrolyde in half cell RMBs [66]. (a) In powder, 0.02 C; (b) MgIn powder, 0.01 C (reproduced with permission).

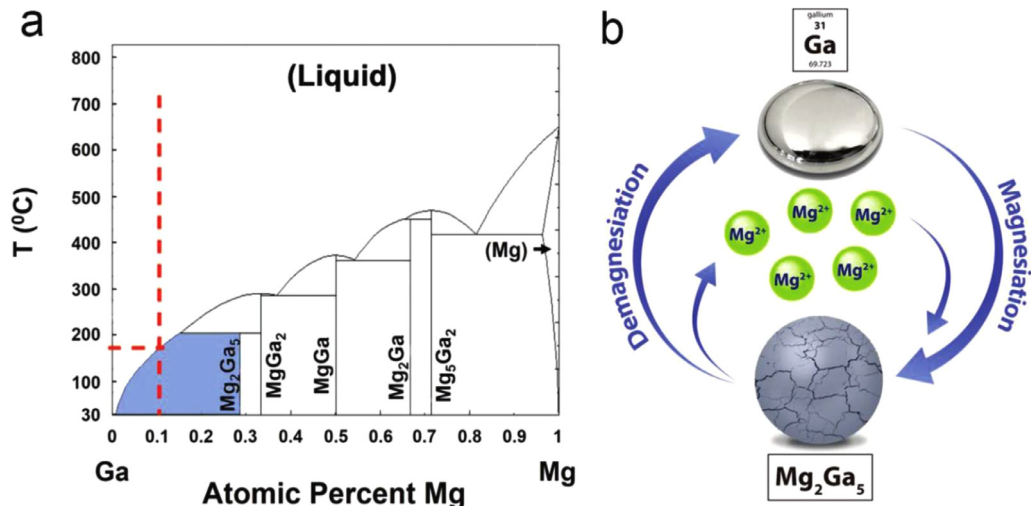


Fig. 14. (a) Equilibrium phase diagram of the Ca-Mg system. (b) Schematic of magnesiation/demagnesiation process during which liquid Ga and solid Mg_2Ga_5 reversibly converted into each other at constant temperature and pressure [69] (reproduced with permission).

3.5. Multi-element alloys

One important hindrance for development of alloy anodes for LIBs is the volume expansion (280 % for $Li_{15}Si_4$ and 244 % for $Li_{17}Sn_4$ against Si and Sn, respectively) during lithiation process [70]. Volume expansion can introduce internal stress to the electrodes and lead to cracks pulverisation of the anode materials during cycling. This will cause fast capacity decay to the total cell. By using multi-element alloys as anodes, more reaction steps will be involved during lithiation/delithiation process thus sudden change of lattice parameters/molar volumes can be avoided. Consequently, internal stress can be reduced and the lifetime of the complete cell can be prolonged. Similar strategy has been applied for the development of alloy anodes for RMBs. The combination of most investigated elements: Bi, Sn, and Sb, have become nature selections.

3.5.1. Bi-Sn alloys

Niu et al. [71] used chemical dealloying of rapid solidified Mg-Bi-Sn alloys to obtain nanoporous (NP) Bi, Bi_6Sn_4 , Bi_4Sn_6 , and Sn alloys starting from $Mg_{90}Bi_{10}$, $Mg_{90}Bi_6Sn_4$,

$Mg_{92}Bi_8$, and $Mg_{90}Sn_{10}$, respectively. NP Bi_6Sn_4 and Bi_4Sn_6 exhibited greatly improved battery performances for both rate capacity and cyclability compare to the NP Bi anode does. Bi_4Sn_6 showed faster capacity decay compare to Bi_6Sn_4 , and Niu et al. [71] attributed it to higher Sn content. Although Bi_6Sn_4 exhibited prior performance than Bi_4Sn_6 , the contribution of Sn to total capacity showed slower fading than that of Bi for the Bi-Sn alloys. After 200 cycles with Bi_6Sn_4 electrode, the capacity fade related to Bi and Sn reactions are 37.9% and 22.7%, respectively. Based on their own results, Niu et al. [71] declared that the duo phase alloy likely “unlocks the kinetic limitation of Sn phase and grants Sn high reversibility to some extent”. By chemical deploying rapidly solidified Al-Bi-Sn with 95 at.% Al content, Niu et al. [72] prepared highly porous NP Bi-Sn alloys, among which the Bi_6Sn_4 composition exhibited the highest reversible capacity, i.e. 353 mA h g⁻¹ and 324 mA h g⁻¹ at current of 100 mA g⁻¹ and 1000 mA g⁻¹, respectively. Fig. 15 shows the currently rate performance of porous alloy electrodes at different rate conditions [72].

Song et al. [73] prepared Bi-Sn alloy film at its eutectic composition using magnetron co-sputtering method. The ob-

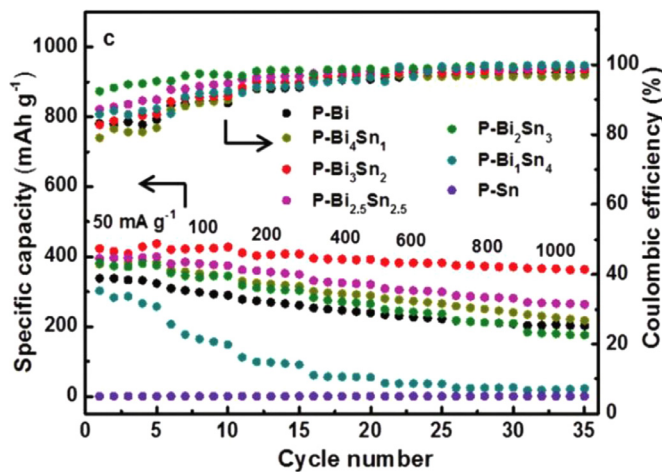
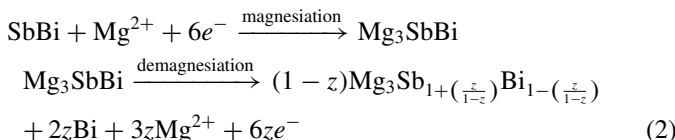


Fig. 15. Rate performance of porous Bi-Sn electrodes at different rate conditions [72] (reproduced with permission).

tained Bi-Sn film delivered high specific capacity (538 mA h g⁻¹ at 50 mA g⁻¹ current), good rate performance (417 mA h g⁻¹ at 1000 mA g⁻¹ current) and cycling stability (233 mA h g⁻¹ in the 200th cycle). Song et al. [74] also prepared Sn-Bi films with different compositions (Sn₉₇Bi₃, Sn₈₂Bi₁₈, Sn₆₇Bi₃₃, Sn₃₃Bi₄) by magnetron co-sputtering and rolling melt alloys and pure Sn. Sn-Bi electrodes demonstrated improved electrochemical performance than pure Sn electrode. Sn₅₃Bi₄₇ electrode could deliver a specific capacity of 200 mA h g⁻¹ at a current of 1000 mA g⁻¹.

3.5.2. Bi-Sb alloys

Although Sb shows little reversible Mg-storage capacity, Sb addition to Bi or Sn can improve their battery performance within RMBs. As reported by Arthur et al. [56] (Fig. 12 (c)), Bi_xSb_{1-x} (x=1, 0.55, 0.88, 0) alloy electrodes delivered 222, 235, 298, and 16 mA h g⁻¹ initial discharge capacity at 1 C rate, respectively. Especially, Bi_{0.88}Sb_{0.12} expressed higher initial capacity compare to pure Bi electrode (see Fig. 12). However, after 100 cycles, the Bi_{0.88}Sb_{0.12} electrode faded to 215 mA h g⁻¹ while Bi anode exhibited 247 mA h g⁻¹ specific capacity. The increased fade progress was attributed to the increased Mg-Sb bond strength compared to Mg-Bi bond [54,75]. However, if we look close to the trend with the Bi_{0.88}Sb_{0.12} and Bi in the Fig. 12 (c), the Bi-Sb alloy may show prior battery performance for prolonged battery tests. This effect could be explained with the phase evolution process of the Bi-Sb alloy proposed by Murgia et al. [76], with an example of SbBi composition given as Eq. (2):



where $0 \leq z \leq 0.5$.

The decomposition of Mg₃SbBi was confirmed by operando XRD. If we look into the microstructure of an alloy

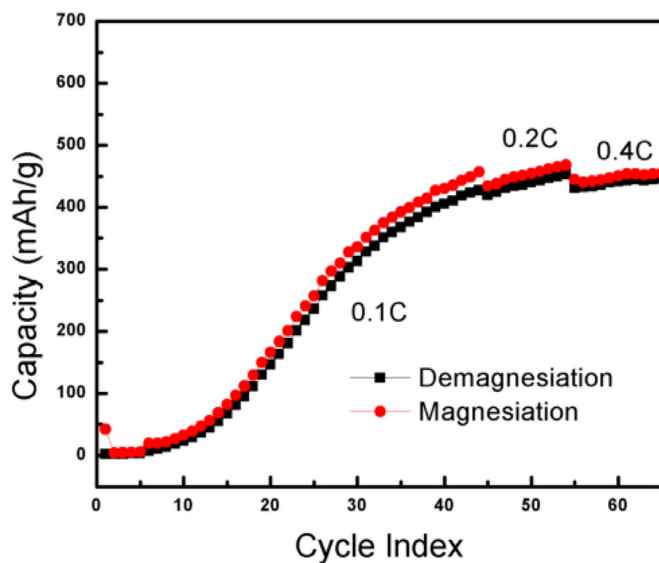


Fig. 16. Charge-discharge profiles of a Mg-SnSb cell tested with the voltage of 0~0.8V (vs. Mg) [77] (reproduced with permission).

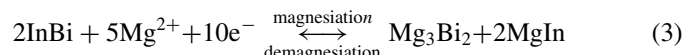
after a eutectoid reaction, very fine even nano-structure can usually be observed. The elevated cyclability was attributed to combination of the eutectoid decompose of Mg₃SbBi and nanostructuration of Bi.

3.5.3. Sb-Sn

Parent et al. [53] used nanosized β -SnSb particles as starting material to build RMBs. After several charge-discharge cycles, the particles irreversibly transformed into Sn and Sb-rich subparticles. In the subsequent following cycles, Sn-rich subparticles showed highly reversible Mg-storage, while Sb-rich subparticles contribute little to the performance. The difficult demagnesiation of Sb was attributed to strong Mg-Sb bond [75]. Nevertheless, the SnSb alloy prepared by Cheng et al. [77] show obvious “activation” process during the magnesiation/demagnesiation process, as shown in Fig. 16. The activation effect was attributed to the formation of porous networks of Sn-rich and Sb-rich subparticles, whose microstructure evolution is given in Fig. 17.

3.5.4. Other alloying elements (In, Cu, Pb)

Murgia et al. [78] prepared InBi compound using high energy ball milling. The obtained InBi compound showed reversible phase conversion reactions during magnesiation/demagnesiation process. For the simply mixed In and Bi powders, only pure elements were observed during demagnetization process without formation of InBi compound. Therefore, the alloying process using high energy ball milling process was critical for the activation of In together with Bi. Total magnesiation/demagnesiation reaction for InBi compound is given as Eq. (3):



The previous results [53,56] suggested that Sb is not a promising anode candidate for RMBs. However, Blondeau

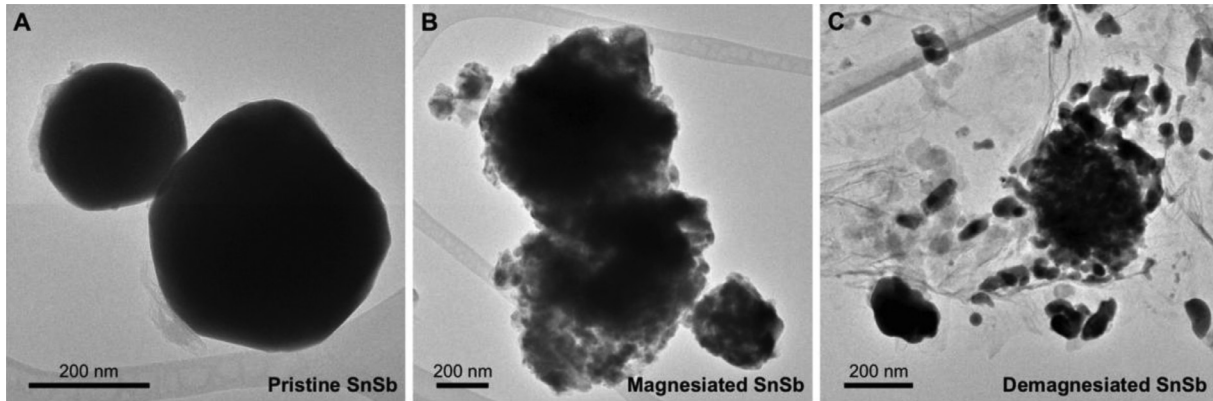


Fig. 17. morphology evolution for SnSb particles in half cell RMB: (a) pristine (b) magnesiated; (c) demagnesiated [77].

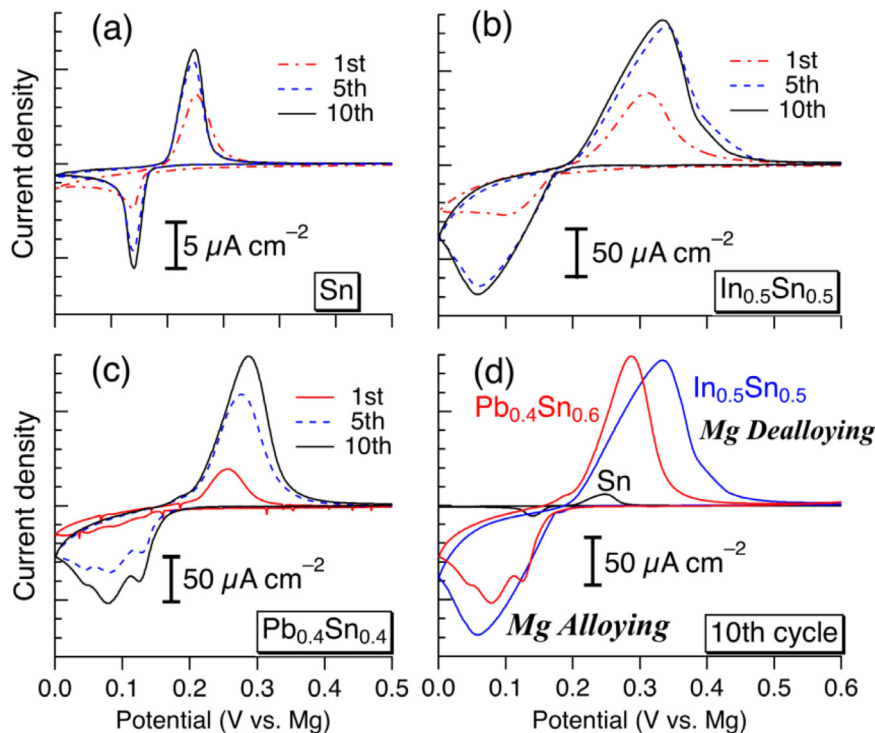


Fig. 18. CV profiles for (a) Sn, (b) Pb_{0.4}Sn_{0.4}, (c) In_{0.5}Sn_{0.5} and (d) the 10th cycle of electrode [80] (reproduced with permission).

et al. [79] recently reported that In can unlock the reversibility of Sb. Blondeau *et al.* prepared InSb compound using ball milling technique. During the first magnesiation process using the InSb compound, only one plateau around 90 mV appeared. However, the characteristic voltage plateau of magnesiation/demagnesiation of Mg₃Sb₂ around 400 mV was observed in the following cycles. This indicates that phase transformations appeared in the electrode. However, XRD results indicated the reformation of InSb compound during the demagnesiation process. Additionally, slow capacity increment was observed in the following cycles, which may be related to ongoing morphology evolution.

Kitada *et al.* [80] investigated Cu-Sn, Pb-Sn, and In-Sn alloys as possible alloy anodes for RMBs. Pb-Sn and In-Sn

alloys showed improved battery capacity and kinetic performance compare to pure Sn electrode, as shown in Fig. 18. Contradictory, Cu-Sn compounds stayed relative inert for the Mg intercalation/deintercalation.

4. Insertion anodes

Beside alloy anodes, which usually include complex phase transformations during magnesiation/demagnesiation process, several intercalation type anodes with which no phase transaction occurs during the battery operations were also proposed.

Several groups have studied carbon-based anode materials for RMBs. Maeda and Touzain [81,82] used highly oriented pyrolytic graphite (HOPG) combined with MgCl₂ dissolved in dimethylsulfoxide (DMSO), and found reversible

Table 1

Summary of experimentally measured specific capacities of alloy anode materials for RMBs. NP – nanopowder; NW – nanowire; NT – nanotube; P – porous.; F - film.

Active material	Counter electrode	Electrolyte	maximum specific capacity, current	Cyclability (capacity retention, current, cycle number)	Rate capability (mA h g ⁻¹), current	Ref
Sn	Mg	(EtMgCl, Et ₂ AlCl)/THF	903 mA h g ⁻¹ , 0.002 C	200 mA h g ⁻¹ , 0.01 C, 10 cycles	200 mA h g ⁻¹ , 0.05 C	[47]
Sn/graphite	Mg	0.4 M APC	280 mA h g ⁻¹ , 50 mA g ⁻¹	110 mA h g ⁻¹ , 50 mA g ⁻¹ , 300 cycles	180 mA h g ⁻¹ , 800 mA g ⁻¹	[77]
Sn	Mg	0.5 M PhMgCl/THF	321 mA h g ⁻¹ , 52 mA g ⁻¹	289 mA h g ⁻¹ , 52 mA g ⁻¹ , 30 cycles		[48]
β -Sn	Mg	0.5 M PhMgCl/THF	8 mA h g ⁻¹ , 10 mA g ⁻¹	7 mA h g ⁻¹ , 10 mA g ⁻¹ , 200 cycles		[49]
NP-Sn	Mg	0.5M EtMgCl/THF	225 mA h g ⁻¹ , 10 mA g ⁻¹	25 mA h g ⁻¹ , 10 mA g ⁻¹ , 50 cycles		[49]
NP – Sn	Mg	0.4 M APC	31 mA h g ⁻¹ , 20 mA g ⁻¹			[71]
P-Sn	Mg	0.4 M APC	380 mA h g ⁻¹ , 5 mA g ⁻¹			[72]
F – Sn	Mg	0.4 M APC	0 mA h g ⁻¹ , 20 mA g ⁻¹			[74]
Mg ₂ Sn	Mg	0.5M PhMgCl/THF	270 mA h g ⁻¹ , 16 mA g ⁻¹	197 mA h g ⁻¹ , 16 mA g ⁻¹ , 50 cycles		[50]
Mg ₂ Sn	Mg	0.4 M APC	300 mA h g ⁻¹ , 180 mA g ⁻¹	280 mA h g ⁻¹ , 180 mA g ⁻¹ , 150 cycles; 1500 mA h g ⁻¹ , 450 mA g ⁻¹ , 150 cycles	180 mA h g ⁻¹ , 450 mA g ⁻¹	[52]
Mg ₂ Sn /graphite	Mg	0.5 M PhMgCl/THF	382 mA h g ⁻¹ , 32 mA g ⁻¹	270 mA h g ⁻¹ , 32 mA g ⁻¹ , 60 cycles	382 mA h g ⁻¹ , 32 mA g ⁻¹	[51]
NP-Sn	MgMn ₂ O ₄	0.5 M Mg(ClO ₄) ₂ /AN	150 mA h g ⁻¹ , 20 mA g ⁻¹	150 mA h g ⁻¹ , 20 mA g ⁻¹ , 20 cycles		[49]
Mg ₂ Sn	Mo ₆ S ₈	(EtMgCl, Et ₂ AlCl)/THF	83 mA h g ⁻¹	46 mA h g ⁻¹ , 10 cycles		[47]
Mg ₃ Sn	Mo ₆ S ₈	0.5 M Mg(TFSI) ₂ /DME	82 mA h g ⁻¹	46 mA h g ⁻¹ , 10 cycles		[47]
Mg ₂ Sn	V ₂ O ₅	0.5 M Mg(TFSI) ₂ /diglyme	149 mA h g ⁻¹ , 8 mA g ⁻¹	104 mA h g ⁻¹ , 8 mA g ⁻¹ , 3 cycles		[50]
Mg ₂ Sn	V ₂ O ₅	0.5 M Mg(TFSI) ₂ /PC	160 mA h g ⁻¹ , 8 mA g ⁻¹	115 mA h g ⁻¹ , 8 mA g ⁻¹ , 3 cycles		[50]
Mg ₂ Sn	V ₂ O ₅	1M Mg(ClO ₄) ₂ /acetonitrile	120 mA h g ⁻¹ , 8 mA g ⁻¹			[50]
NP - Bi (18 nm)	Mg	0.2 M / 2 M Mg(BH ₄) ₂ /LiBH ₄ in diglyme	335 mA h g ⁻¹ , 192 mA g ⁻¹	315 mA h g ⁻¹ , 770 mA g ⁻¹ , 150 cycles; 150 mA h g ⁻¹ , 7700 mA g ⁻¹ , 4500 cycles	280 mA h g ⁻¹ , 7700 mA g ⁻¹	[62]
NP - Bi (10 nm)	Mg	0.2 M / 2 M Mg(BH ₄) ₂ /LiBH ₄ in diglyme	310 mA h g ⁻¹ , 192 mA g ⁻¹	290 mA h g ⁻¹ , 770 mA g ⁻¹ , 150 cycles	180 mA h g ⁻¹ , 7700 mA g ⁻¹	[62]
Bi	Mg	0.2 M / 2 M Mg(BH ₄) ₂ /LiBH ₄ in diglyme	325 mA h g ⁻¹ , 192 mA g ⁻¹	170 mA h g ⁻¹ , 770 mA g ⁻¹ , 150 cycles	150 mA h g ⁻¹ , 7700 mA g ⁻¹	[62]
Bi	Mg	2 M EtMgCl/THF	326 mA h g ⁻¹ , 20 mA g ⁻¹	285 mA h g ⁻¹ , 20 mA g ⁻¹ , 50 cycles	1 mA h g ⁻¹ , 700 mA g ⁻¹	[63]
NT - Bi	Mg	0.1 M / 1.5 M Mg(BH ₄) ₂ /LiBH ₄ in diglyme	350 mA h g ⁻¹ , 0.05 C	303 mA h g ⁻¹ , 200 cycles	216 mA h g ⁻¹ , 5 C	[58]
Bi	Mg	0.1 M / 1.5 M Mg(BH ₄) ₂ /LiBH ₄ in diglyme	350 mA h g ⁻¹ , 0.05 C	188 mA h g ⁻¹ , 200 cycles	51 mA h g ⁻¹ , 5 C	[58]
NP - Bi	Mg	0.1 M / 1.5 M Mg(BH ₄) ₂ /LiBH ₄ in diglyme	350 mA h g ⁻¹ , 0.2 C	260 mA h g ⁻¹ , 1 C, 200 cycles	122 mA h g ⁻¹ , 5 C	[58]
Bi	Mg	0.25 M EtMgCl- (Et ₂ AlCl) ₂ /THF	371 mA h g ⁻¹ , 0.2 C		300 mA h g ⁻¹ , 1 C	[60]
Bi	Mg	(EtMgCl, Et ₂ AlCl)/THF	330 mA h g ⁻¹ , 0.01 C	222 mA h g ⁻¹ , 1 C, 100 cycles		[56]
Bi	Mg	(EtMgCl, Et ₂ AlCl)/THF	385 mA h g ⁻¹ , 0.002 C		270 mA h g ⁻¹ , 0.05 C	[47]
P - Bi	Mg	0.4 M APC	309 mA h g ⁻¹ , 100 mA g ⁻¹	40 mA h g ⁻¹ , 200 mA g ⁻¹ , 100 cycles	200 mA h g ⁻¹ , 1000 mA g ⁻¹	[72]
NW - Bi	Mg	0.25 M Mg(AlCl ₂ BuEt ₂) ₂ /THF	353 mA h g ⁻¹ , 19.25 mA g ⁻¹	207 mA h g ⁻¹ , 192.5 mA g ⁻¹ , 100 cycles		[59]

(continued on next page)

Table 1 (continued)

Active material	Counter electrode	Electrolyte	maximum specific capacity, current	Cyclability (capacity retention, current, cycle number)	Rate capability (mA h g ⁻¹), current	Ref
Bi	Mg	0.35 M (EtMgCl, Et ₂ AlCl)/THF	370 mA h g ⁻¹ , 12.8 mA	300 mA h g ⁻¹ , 2 C, 50 cycles	220 mA h g ⁻¹ , 5 C	[55]
Bi	Mg	0.25 M EtMgCl-(Et ₂ AlCl) ₂ /THF	330 mA h g ⁻¹ , 0.05 C		300 mA h g ⁻¹ , 1 C	[61]
NP - Bi	Mg	0.4 M APC	330 mA h g ⁻¹ , 50 mA	43 mA g ⁻¹ , 200 mA	7 mA h g ⁻¹ , 1000 mA	[71]
NP - Mg ₃ Bi ₂	Mg	LiCl-APC	360 mA h g ⁻¹ , 100 mA	263 mA h g ⁻¹ , 100 mA	251 mA h g ⁻¹ , 1900 mA g ⁻¹	[65]
			g ⁻¹	g ⁻¹ , 200 cycles; 209 mA h g ⁻¹ , 380 mA	g ⁻¹ , 300 cycles	
Bi _{0.95} RGO _{0.05}	Mg	2M EtMgCl/THF	333 mA h g ⁻¹ , 15 mA	222 mA h g ⁻¹ , 15 mA		[63]
Bi _{0.8} RGO _{0.2}	Mg	2M EtMgCl/THF	338 mA h g ⁻¹ , 29 mA	299 mA h g ⁻¹ , 29 mA		[63]
Bi _{0.7} RGO _{0.3}	Mg	2M EtMgCl/THF	363 mA h g ⁻¹ , 24 mA	304 mA h g ⁻¹ , 24 mA		[63]
Bi _{0.6} RGO _{0.4}	Mg	2M EtMgCl/THF	413 mA h g ⁻¹ , 39 mA	372 mA h g ⁻¹ , 39 mA	238 mA h g ⁻¹ , 700 mA	[63]
Bi _{0.5} RGO _{0.5}	Mg	2M EtMgCl/THF	350 mA h g ⁻¹ , 33 mA	307 mA h g ⁻¹ , 33 mA		[63]
			g ⁻¹	g ⁻¹ , 50 cycles	g ⁻¹	
N - Bi	Mo ₆ S ₈	0.25 M Mg(TFSI) ₂ in diglyme	285 mA h g ⁻¹ , 384 mA	285 mA h g ⁻¹ , 384 mA		[62]
N-Bi	Mo ₆ S ₈	0.2 M / 2 M Mg(BH ₄) ₂ /LiBH ₄ in diglyme	310 mA h g ⁻¹ , 384 mA	310 mA h g ⁻¹ , 384 mA		[62]
Mg ₃ Bi ₂	Mo ₆ S ₈	0.4 M Mg(TFSI) ₂ /diglyme	89 mA h g ⁻¹ , 0.1 C	62 mA h g ⁻¹ , 20 cycles		[58]
Mg ₃ Bi ₂	Mo ₆ S ₈	0.1 M /1.5 M Mg(BH ₄) ₂ /LiBH ₄ in diglyme	92 mA h g ⁻¹ , 0.2 C	65 mA h g ⁻¹ , 20 cycles		[58]
NP - Mg ₃ Bi ₂	Prussian Blue	2 M /1 M Mg(TFSI) ₂ /LiTFSI/AN	103 mA h g ⁻¹ , 100 mA	92 mA h g ⁻¹ , 200 mA	58 mA h g ⁻¹ , 2000 mA	[65]
NP - Mg ₃ Bi ₂	V ₂ O ₅	2 M Mg(TFSI) ₂ -/1 M LiTFSI/AN	268 mA h g ⁻¹ , 200 mA	180 mA h g ⁻¹ , 200 mA		[65]
NP - Mg ₃ Bi ₂	birnessite-MnO ₂	2 M Mg(TFSI) ₂ -/1 M LiTFSI/AN	107 mA h g ⁻¹ , 200 mA	55 mA h g ⁻¹ , 200 mA		[65]
BiOF	Mg	0.25 M Mg(AlCl ₂ BuEt ₂) ₂ /THF	353 mA h g ⁻¹ , 15 mA	255 mA h g ⁻¹ , 300 mA	273 mA h g ⁻¹ , 300 mA	[64]
Sb	Mg	(EtMgCl, Et ₂ AlCl)/THF	660 mA h g ⁻¹ , 0.01 C	16 mA h g ⁻¹ , 1 C, 50 cycles		[56]
In	Mg	0.35 M (EtMgCl, Et ₂ AlCl)/THF	460 mA h g ⁻¹ , 0.02 C	425 mA h g ⁻¹ , 0.02 C, 10 cycles	280 mA h g ⁻¹ , 0.1 C	[66]
MgIn	Mg	0.35 M (EtMgCl, Et ₂ AlCl)/THF	355 mA h g ⁻¹ , 0.01 C	340 mA h g ⁻¹ , 0.01 C, 6 cycles		[66]
Pb (60°C)	Mg foil	0.5 M EtMgCl-0.25 M AlCl ₃ /THF	380 mA h g ⁻¹ , 0.025 C	275 mA h g ⁻¹ , 0.025 C, 10 cycles		[54]
F - Pb film (60°C)	Mg foil	0.5 M EtMgCl-0.25 M AlCl ₃ /THF	517 mA h g ⁻¹ , 0.025 C	450 mA h g ⁻¹ , 0.025 C, 13 cycles		[54]
Mg ₂ Ga ₅ (40°C)	Mg	0.4 M APC + 0.4 M LiCl	306 mA h g ⁻¹ , 615 mA	289.5 mA h g ⁻¹ , 615 mA g ⁻¹ , 680 cycles; 212.7 mA h g ⁻¹ , 922.5 mA g ⁻¹ , 1000 cycles	270 mA h g ⁻¹ , 615 mA	[69]
Eutectic Bi-Sn	Mg	0.4 M APC	528 mA h g ⁻¹ , 50 mA	233 mA g ⁻¹ , 1000 mA	417 mA h g ⁻¹ , 1000 mA g ⁻¹	[73]
			g ⁻¹	g ⁻¹ , 200 cycles; 182 mA g ⁻¹ , 3000 mA	g ⁻¹ , 200 cycles;	
F - Sn ₉₇ Bi ₃	Mg	0.4 M APC	220 mA h g ⁻¹ , 20 mA	20 mA h g ⁻¹ , 20 mA	25 mA h g ⁻¹ , 1000 mA	[74]
F - Sn ₉₃ Bi ₇	Mg	0.4 M APC	320 mA h g ⁻¹ , 20 mA	30 mA h g ⁻¹ , 20 mA	45 mA h g ⁻¹ , 1000 mA	[74]
			g ⁻¹	g ⁻¹ , 20 cycles	g ⁻¹	

(continued on next page)

Table 1 (continued)

Active material	Counter electrode	Electrolyte	maximum specific capacity, current	Cyclability (capacity retention, current, cycle number)	Rate capability (mA h g ⁻¹), current	Ref
F – Sn ₈₂ Bi ₁₈	Mg	0.4 M APC	600 mA h g ⁻¹ , 20 mA g ⁻¹	40 mA h g ⁻¹ , 20 mA g ⁻¹ , 25 cycles	120 mA h g ⁻¹ , 1000 mA g ⁻¹	[74]
F – Sn ₆₇ Bi ₃₃	Mg	0.4 M APC	370 mA h g ⁻¹ , 20 mA g ⁻¹	45 mA h g ⁻¹ , 20 mA g ⁻¹ , 50 cycles	175 mA h g ⁻¹ , 1000 mA g ⁻¹	[74]
F – Sn ₅₃ Bi ₄₇	Mg	0.4 M APC	500 mA h g ⁻¹ , 20 mA g ⁻¹	108 mA h g ⁻¹ , 20 mA g ⁻¹ , 80 cycles	200 mA h g ⁻¹ , 1000 mA g ⁻¹	[74]
P – Bi ₄ Sn ₁	Mg	0.4 M APC	361 mA h g ⁻¹ , 100 mA g ⁻¹	130 mA h g ⁻¹ , 200 mA g ⁻¹ , 100 cycles	230 mA h g ⁻¹ , 1000 mA g ⁻¹	[72]
P – Bi ₃ Sn ₂	Mg	0.4 M APC	416 mA h g ⁻¹ , 100 mA g ⁻¹	305 mA h g ⁻¹ , 1000 mA g ⁻¹ , 200 cycles	367 mA h g ⁻¹ , 1000 mA g ⁻¹	[72]
P – Bi _{2.5} Sn _{2.5}	Mg	0.4 M APC	380 mA h g ⁻¹ , 100 mA g ⁻¹	215 mA h g ⁻¹ , 200 mA g ⁻¹ , 100 cycles	270 mA h g ⁻¹ , 1000 mA g ⁻¹	[72]
P – Bi ₂ Sn ₃	Mg	0.4 M APC	353 mA h g ⁻¹ , 100 mA g ⁻¹	230 mA h g ⁻¹ , 200 mA g ⁻¹ , 100 cycles	210 mA h g ⁻¹ , 1000 mA g ⁻¹	[72]
P – Bi ₁ Sn ₄	Mg	0.4 M APC	206 mA h g ⁻¹ , 100 mA g ⁻¹	20 mA h g ⁻¹ , 200 mA g ⁻¹ , 100 cycles	20 mA h g ⁻¹ , 1000 mA g ⁻¹	[72]
NP – Bi ₆ Sn ₄	Mg	0.4 M APC	434 mA h g ⁻¹ , 50 mA g ⁻¹	280 mA h g ⁻¹ , 200 mA g ⁻¹ , 200 cycles;	362 mA h g ⁻¹ , 1000 mA g ⁻¹	[71]
NP – Bi ₄ Sn ₆	Mg	0.4 M APC	482 mA h g ⁻¹ , 50 mA g ⁻¹	220 mA h g ⁻¹ , 200 mA g ⁻¹ , 200 cycles;	260 mA h g ⁻¹ , 1000 mA g ⁻¹	[71]
SnSb/graphite	Mg	0.4 M APC	420 mA h g ⁻¹ , 50 mA g ⁻¹	270 mA h g ⁻¹ , 500 mA g ⁻¹ , 200 cycles	300 mA h g ⁻¹ , 1000 mA g ⁻¹	[77]
SnSb/graphite	Mg	0.4 M APC + 0.5 M LiCl	460 mA h g ⁻¹ , 50 mA g ⁻¹		400 mA h g ⁻¹ , 1000 mA g ⁻¹	[77]
SnSb/graphite	Mg	APC	420 mA h g ⁻¹ , 50 mA g ⁻¹	260 mA h g ⁻¹ , 50 mA g ⁻¹ , 200 cycles		[53]
SnSb/graphite	Mo ₆ S ₈	0.4 M APC	75 mA h g ⁻¹ , 0.1 C	70 mA h g ⁻¹ , 0.1 C, 15 cycles		[77]
SnSb/graphite	Mo ₆ S ₈	0.5 M Mg(TFSI) ₂ /diglyme	75 mA h g ⁻¹ , 0.1 C	60 mA h g ⁻¹ , 0.1 C, 16 cycles		[77]
Bi _{0.88} Sb _{0.12}	Mg	(EtMgCl,Et ₂ AlCl)/THF	380 mA h g ⁻¹	215 mA h g ⁻¹ , 1 C, 100 cycles		[56]
Bi _{0.55} Sb _{0.45}	Mg	(EtMgCl,Et ₂ AlCl)/THF	420 mA h g ⁻¹	151 mA h g ⁻¹ , 1 C, 100 cycles		[56]
InSb	Mg	0.35 M (EtMgCl,Et ₂ AlCl)/THF	530 mA h g ⁻¹ , 5.5 mA g ⁻¹	350 mA h g ⁻¹ , 11 mA g ⁻¹ , 45 cycles	200 mA h g ⁻¹ , 22 mA g ⁻¹ ; 0 mA h g ⁻¹ , 550 mA g ⁻¹	[79]
InBi	Mg	0.35 M (EtMgCl,Et ₂ AlCl)/THF	410 mA h g ⁻¹ , 0.01 C	280 mA h g ⁻¹ , 0.05 C, 100 cycles;	150 mA h g ⁻¹ , 1 C; 0 mA h g ⁻¹ , 2 C	[78]

electrochemical insertion of Mg²⁺ into the HOPG. Kim et al. [83] investigated cointercalation of Mg²⁺ ions into natural graphite with linear ether solvents, diethylene glycol dimethyl ether (DEGDME) and 1,2-dimethoxyethane (DME) experimentally and performed ab initio calculation to show DEGDME is the most advantageous for cointercalation due to its high binding energy with Mg²⁺ ions (10.05 eV). Er et al. [84] studied the adsorption of divalent Mg ions on defective graphene and graphene allotropes by first-principles density functional theory. A theoretical capacity up to 1042 mA h g⁻¹ was proposed with graphene including 25% divacancy defects. Lim et al. [85] prepared three-dimensional macroporous graphitic carbon nanosubstrates which demonstrated improved rate capacity as well as cyclabilities.

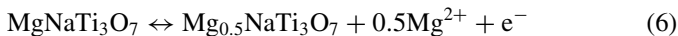
Although the usage of carbon-based material facilitate the electrolyte adoption, low specific charge and short cycle could

happen due to the co-insertion process of solvent molecules (solv) as shown in Eq. (4) [86]. Therefore, following investigations are required, especially on the cycle life aspect.



Chen et al. [87] applied Na₂Ti₃O₇ as anode material RMB. During the first magnesiation process, Mg substituted half of the Na positions in Na₂Ti₃O₇ following reaction (5). Afterward, half amount of the Mg integrations could be reversibly inserted & extracted following reaction (6). Na₂Ti₃O₇ delivered reversible capacity of 78 mA h g⁻¹ (theoretical capacity 88 mA h g⁻¹) for over 100 cycles under 20 mA g⁻¹ current. It also demonstrated good rate performance up to 1000 mA g⁻¹ current, under which the reversible capacity was 40 mA h g⁻¹. Furthermore, full Mg-ion batteries (MgNaTi₃O₇/Mg-

$\text{Mg}(\text{ClO}_4)_2$ -diglyme/ V_2O_5) delivered an energy density of 53 Wh kg⁻¹.



Wu et al. [88] assembled battery using Mg and $\text{Li}_4\text{Ti}_5\text{O}_{12}$ electrodes with $\text{Mg}(\text{AlCl}_2\text{BuEt}_2)_2/\text{THF}$ electrolyte. A reversible capacity around 175 mA h g⁻¹ was obtained under 15 mA g⁻¹ current. During the charge process, Li atoms were extracted from 8a sites of $\text{Li}_4\text{Ti}_5\text{O}_{12}$. During the following discharge process Mg atoms entered empty 8a sites which was originally occupied by Li atoms. Some Mg atoms also entered previously empty 16c sites. By adding 0.25 M LiCl into the $\text{Mg}(\text{AlCl}_2\text{BuEt}_2)_2/\text{THF}$ electrode, $\text{Li}_4\text{Ti}_5\text{O}_{12}$ delivered reversible capacity around 175 mA h g⁻¹ with small capacity decay of 0.01% per cycle for over 500 cycles. With the addition of LiCl to the system, $\text{Li}_4\text{Ti}_5\text{O}_{12}$ could deliver a reversible capacity around 120 mA h g⁻¹ under current rate of 300 mA g⁻¹. While without LiCl addition, only around 50 mA h g⁻¹ could be obtained under the same conditions. The improved battery performance was attributed to co-intercalation of Li and Mg into $\text{Li}_4\text{Ti}_5\text{O}_{12}$ electrode. [89].

Zeng et al. [90] firstly reported the possibility of using Li_3VO_4 as the insertion type anode for RMBs. However, the Mg insertion kinetic is sluggish with Li_3VO_4 material. To conquer this problem, Zen *et al.* applied mesoporous $\text{Li}_3\text{VO}_4/\text{C}$ hollow spheres, obtained 318 mA h g⁻¹ for the first cycle, and maintained 57 % at the 15th cycle. Black phosphorus was also predicated to be able to deliver a high capacity as well as high rate capacity due to the covalent Mg-P bonding [91].

5. Summary and perspectives

RMBs have attracted constantly increasing attention as one of the most promising post lithium battery systems. Because of the possibility of using pure Mg as the anode material, most studies focus on the development of advanced cathode materials. However, a good cathode material must combine with compatible anode and electrolyte for its full usability. The widely studied Grignard-based electrolyte solutions are compatible with pure Mg anodes without formation of thick passive layers. However, the Grignard-based electrolyte solutions are limited by narrow voltage window as well as toxicity. The newly developed fluorinated alkoxyborate-based electrolytes exhibited a high anodic stability, high ionic conductivity and high coulombic efficiency of magnesium deposition. However, high-performance anodes beside pure Mg are always demanded to further broad the choice of usable electrolytes, cathodes, as well as other cell components.

The most investigated alternative anodes for RMBs are alloy anodes based on Bi, Sn, Sb, In, Pb etc., where Bi and Sn seem to be more promising than the others. These alloy anodes allow usage of conventional electrolytes, but also have shortages such as slow Mg²⁺ transport and significant vol-

ume change during magnesiation/demagnesiation process. The slow kinetics can be overcome by reducing particle size or by modifying the morphology. The volume change is mostly combined with phase transformation, which means both crystal structure and molar volume of formed intermetallic phases change drastically at certain compositions during the battery operations. The drastic volume change usually leads to pulverization of the anode materials and battery capacity fading for LIBs. In contradictory, the volume change often causes formation of continuous nanopores instead of pulverization for RMB alloy anodes. This nanomerization process can improve Mg²⁺ transportation inside the anode part as well as cyclability of the entire cell. Additionally, it can be enhanced by combining different alloy elements, e.g. by adding Sb or In into Bi or Sn, resulted from variation of phase transformation sequences. Initial morphology of the anode materials can also greatly influence their subsequent performance. Therefore, multi-element alloy anodes with carefully designed initial morphology and reaction routine may further enhance the performance of alloy anodes for RMBs. Additionally, the novel Ga anode, which involves liquid phase during cycling process, demonstrated the possibility of self-healing for RMB alloy anodes. The reported specific capacity, rate capacity, and cyclability of alloy anodes for RMBs are summarized in Table 1.

Although fewer studies than alloy anodes were reported, insertion anodes already showed promising potential for RMBs with various mechanisms. Mg²⁺ can be inserted/extracted with Li_3VO_4 anode material, which may be enhanced by doping in future studies. Besides development of complete new materials, doping with elements offers further potential for improving the already found anode materials.

During the first several “demagnesiation” process, Na in $\text{Na}_2\text{Ti}_3\text{O}_7$ or Li in $\text{Li}_4\text{Ti}_5\text{O}_{12}$ can be partially extracted from the initial materials. Given proper Mg sources, Mg ions will refill the left vacancies during the next magnesiation process. The implanted Mg ions stay active in the following cycles to provide reversible cyclability for the entire RMBs. The Mg-containing anodes after the substitution process are most likely in metastable states, which can hardly be obtained through normal synthesis process. Therefore, this substitution process provides a unique direction for extending the selection range of RMBs anodes. However, long-term electrochemical tests are required to validate the stability of the substituted anodes for RMBs.

In summary, although anodes are less reported than cathodes or electrolytes for the RMBs, this doesn't mean that the corresponding studies should be abandoned. In contrast, development of high-performance anodes is essential for the future of novel RMBs. More studies on looking for potential host materials as well as proper combinations with other battery components are highly demanded.

Acknowledgments

This work is financially supported by the German Research Foundation DFG project (LI 2839/1-1) and National Natu-

ral Science Foundation of China (51971044). MF acknowledges funding from EU research and innovation framework programme via “E-MAGIC” project (ID: 824066). This work contributes to the research performed at CELEST (Center for Electrochemical Energy Storage Ulm-Karlsruhe).

References

- [1] J.M. Tarascon, M. Armand, *Nature* 414 (6861) (2001) 359–367.
- [2] J.B. Goodenough, K.-S. Park, *J. Am. Chem. Soc.* 135 (4) (2013) 1167–1176.
- [3] J. Thomas, *Nat. Mater.* 2 (11) (2003) 705–706.
- [4] N. Nitta, F.X. Wu, J.T. Lee, G. Yushin, *Mater. Today* 18 (5) (2015) 252–264.
- [5] M.S. Whittingham, *Chem. Rev.* 114 (23) (2014) 11414–11443.
- [6] D. Andre, S.J. Kim, P. Lamp, S.F. Lux, F. Maglia, O. Paschos, B. Stiasny, *J. Mater. Chem. A* 3 (13) (2015) 6709–6732.
- [7] E.M. Sarkar, T. Sarkar, M.D. Bharadwaj, *Curr. Sci. India* 114 (12) (2018) 2453–2458.
- [8] J.Y. Hwang, S.T. Myung, Y.K. Sun, *Chem. Soc. Rev.* 46 (12) (2017) 3529–3614.
- [9] L. Cailloce, A battery revolution in motion, 2015. <https://news.cnrs.fr/articles/a-battery-revolution-in-motion>.
- [10] A. Ponrouch, J. Bitenc, R. Dominko, N. Lindahl, P. Johansson, M.R. Palacin, *Energy Storage Mater.* (2019).
- [11] H.D. Yoo, I. Shterenberg, Y. Gofer, G. Gershinsky, N. Pour, D. Aurbach, *Energy Environ. Sci.* 6 (8) (2013) 2265–2279.
- [12] M. Fichtner, *R. Soc. Chem.* (2020).
- [13] D. Aurbach, Z. Lu, A. Schechter, Y. Gofer, H. Gizbar, R. Turgeman, Y. Cohen, M. Moshkovich, E. Levi, *Nature* 407 (6805) (2000) 724–727.
- [14] J. Song, J. She, D. Chen, F. Pan, J. Magnes. Alloys 8 (1) (2020) 1–41.
- [15] T.D. Gregory, R.J. Hoffman, R.C. Winterton, *J. Electrochem. Soc.* 137 (3) (1990) 775–780.
- [16] M.L. Mao, T. Gao, S.Y. Hou, C.S. Wang, *Chem. Soc. Rev.* 47 (23) (2018) 8804–8841.
- [17] P. Canepa, G.S. Gautam, D.C. Hannah, R. Malik, M. Liu, K.G. Gallagher, K.A. Persson, G. Ceder, *Chem. Rev.* 117 (5) (2017) 4287–4341.
- [18] M. Rashad, M. Asif, I. Ahmed, Z. He, L. Yin, Z.X. Wei, Y. Wang, J. Magnes. Alloys 8 (2) (2020) 364–373.
- [19] R. Attias, M. Salama, B. Hirsch, Y. Goffer, D. Aurbach, *Joule* 3 (1) (2019) 27–52.
- [20] H. Wang, X. Feng, Y. Chen, Y.-S. Liu, K.S. Han, M. Zhou, M.H. Engelhard, V. Murugesan, R.S. Assary, T.L. Liu, W. Henderson, Z. Nie, M. Gu, J. Xiao, C. Wang, K. Persson, D. Mei, J.-G. Zhang, K.T. Mueller, J. Guo, K. Zavadil, Y. Shao, J. Liu, *ACS Energy Lett.* 5 (1) (2020) 200–206.
- [21] Z. Zhao-Karger, M.E. Gil Bardaji, O. Fuhr, M. Fichtner, *J. Mater. Chem. A* 5 (22) (2017) 10815–10820.
- [22] Z. Zhao-Karger, M. Fichtner, *Front. Chem.* 6 (656) (2019).
- [23] Z. Ma, D.R. MacFarlane, M. Kar, *Batter. Supercaps* 2 (2) (2019) 115–127.
- [24] C.M. MacLaughlin, *ACS Energy Lett.* 4 (2) (2019) 572–575.
- [25] K. Jayasyae, R. Rerthelot, K.C. Lethesh, E.M. Sheridan, Anode materials for rechargeable Mg batteries, in: M. Fichtner (Ed.), *Magnesium Batteries Research and Applications* Royal Society of Chemistry, 2019, pp. 114–141.
- [26] J. Niu, Z. Zhang, D. Aurbach, *Adv. Energy Mater.* 10 (23) (2020) 2000697.
- [27] P. Bonnick, J. Muldoon, *Adv. Funct. Mater.* 30 (21) (2020) 1910510.
- [28] R. Davidson, A. Verma, D. Santos, F. Hao, C. Fincher, S. Xiang, J. Van Buskirk, K. Xie, M. Pharr, P.P. Mukherjee, S. Banerjee, *ACS Energy Lett.* 4 (2) (2019) 375–376.
- [29] Z. Lu, A. Schechter, M. Moshkovich, D. Aurbach, *J. Electroanal. Chem.* 466 (2) (1999) 203–217.
- [30] Y.L. Liang, R.J. Feng, S.Q. Yang, H. Ma, J. Liang, J. Chen, *Adv. Mater.* 23 (5) (2011) 640.
- [31] S.-B. Son, T. Gao, S.P. Harvey, K.X. Steirer, A. Stokes, A. Norman, C. Wang, A. Cresce, K. Xu, C. Ban, *Nat. Chem.* 10 (5) (2018) 532–539.
- [32] R. Lv, X. Guan, J. Zhang, Y. Xia, J. Luo, *Natl. Sci. Rev.* 7 (2) (2020) 333–341.
- [33] J. Zhang, X. Guan, R. Lv, D. Wang, P. Liu, J. Luo, *Energy Storage Mater.* 26 (2020) 408–413.
- [34] Y.K. Zhang, S.J. Liao, Y.H. Fan, J. Xu, F.D. Wang, J. Nanopart. Res. 3 (1) (2001) 23–26.
- [35] T. Zheng, Y. Hu, S. Yang, J. Magnes. Alloys 5 (4) (2017) 404–411.
- [36] W. Li, C. Li, C. Zhou, H. Ma, J. Chen, *Angew. Chem. Int. Ed.* 45 (36) (2006) 6009–6012.
- [37] X.Y. Yan, F. Zhang, Y.A. Chang, *J. Phase Equilib.* 21 (4) (2000) 379–384.
- [38] H.L. Yan, Y. Du, L.C. Zhou, H.H. Xu, L.J. Zhang, S.H. Liu, *Int. J. Mater. Res.* 101 (12) (2010) 1489–1496.
- [39] F.G. Meng, J. Wang, L.B. Liu, Z.P. Jin, *J. Alloys Compd.* 508 (2) (2010) 570–581.
- [40] O.I. Malyi, T.L. Tan, S. Manzhos, *J. Power Sources* 233 (2013) 341–345.
- [41] R.A. Huggins, *Advanced Batteries Materials Science Aspects*, Springer Science+Business Media, New York, 2009.
- [42] M. Wang, J.A. Yuwono, V. Vasudevan, N. Birbilis, N.V. Medhekar, *Acs Appl. Mater. Interfaces* 11 (1) (2019) 774–783.
- [43] Z. Wang, Q. Su, J. Shi, H. Deng, G.Q. Yin, J. Guan, M.P. Wu, Y.L. Zhou, H.L. Lou, Y.Q. Fu, *Acs Appl. Mater. Interfaces* 6 (9) (2014) 6786–6789.
- [44] W. Jin, Z. Li, Z. Wang, Y.Q. Fu, *Mater. Chem. Phys.* 182 (2016) 167–172.
- [45] W. Jin, Z. Wang, *RSC Adv.* 7 (70) (2017) 44547–44551.
- [46] W. Jin, Z.G. Wang, *Mater. Chem. Phys.* 217 (2018) 388–392.
- [47] N. Singh, T.S. Arthur, C. Ling, M. Matsui, F. Mizuno, *Chem. Commun.* 49 (2) (2013) 149–151.
- [48] D.-T. Nguyen, X.M. Tran, J. Kang, S.-W. Song, *ChemElectroChem* 3 (11) (2016) 1813–1819.
- [49] F. Nacimiento, M. Cabello, C. Perez-Vicente, R. Alcantara, P. Lavela, G.F. Ortiz, J.L. Tirado, *Nanomaterials* 8 (7) (2018) 501–510.
- [50] D.-T. Nguyen, S.-W. Song, *J. Power Sources* 368 (2017) 11–17.
- [51] G.T.H. Nguyen, D.-T. Nguyen, S.-W. Song, *Adv. Mater. Interfaces* 5 (22) (2018) 1801039.
- [52] H.Y. Asl, J.T. Fu, H. Kumar, S.S. Welborn, V.B. Shenoy, E. Detsi, *Chem. Mater.* 30 (5) (2018) 1815–1824.
- [53] L.R. Parent, Y. Cheng, P.V. Sushko, Y. Shao, J. Liu, C.-M. Wang, N.D. Browning, *Nano Lett.* 15 (2) (2015) 1177–1182.
- [54] K. Periyappuruma, T.T. Tran, M.I. Purcell, M.N. Obrovac, *Electrochim. Acta* 165 (2015) 162–165.
- [55] F. Murgia, L. Stievano, L. Monconduit, R. Berthelot, *J. Mater. Chem. A* 3 (32) (2015) 16478–16485.
- [56] T.S. Arthur, N. Singh, M. Matsui, *Electrodeposited Bi*, *Electrochim. Commun.* 16 (1) (2012) 103–106.
- [57] R.A. DiLeo, Q. Zhang, A.C. Marschilok, K.J. Takeuchi, E.S. Takeuchi, *ECS Electrochem. Lett.* 4 (1) (2015) A10–A14.
- [58] Y. Shao, M. Gu, X. Li, Z. Nie, P. Zuo, G. Li, T. Liu, J. Xiao, Y. Cheng, C. Wang, J.-G. Zhang, J. Liu, *Nano Lett.* 14 (1) (2014) 255–260.
- [59] Z.G. Liu, J. Lee, G.L. Xiang, H.F.J. Glass, E.N. Keyzer, S.E. Dutton, C.P. Grey, *Chem. Commun.* 53 (4) (2017) 743–746.
- [60] A. Benmayza, M. Ramanathan, N. Singh, F. Mizuno, J. Prakash, *J. Electrochem. Soc.* 162 (8) (2015) A1630–A1635.
- [61] M. Ramanathan, A. Benmayza, J. Prakash, N. Singh, F. Mizuno, *J. Electrochem. Soc.* 163 (3) (2016) A477–A487.
- [62] K.V. Kravchyk, L. Piyeteau, R. Caputo, M. He, N.P. Stadie, M.I. Bodnaruk, R.T. Lechner, M.V. Kovalenko, *Acs Nano* 12 (8) (2018) 8297–8307.
- [63] T.R. Penki, G. Valuroothu, S. Shivakumara, V.A. Sethuraman, N. Muchandraiah, *New J. Chem.* 42 (8) (2018) 5996–6004.
- [64] W. Wang, L. Liu, P.F. Wang, T.T. Zuo, Y.X. Yin, N. Wu, J.M. Zhou, Y. Wei, Y.G. Guo, *Chem. Commun.* 54 (14) (2018) 1714–1717.
- [65] Y.-H. Tan, W.-T. Yao, T. Zhang, T. Ma, L.-L. Lu, F. Zhou, H.-B. Yao, S.-H. Yu, *ACS Nano* 12 (6) (2018) 5856–5865.

- [66] F. Murgia, E.T. Weldekidan, L. Stievano, L. Monconduit, R. Berthelot, *Electrochim. Commun.* 60 (2015) 56–59.
- [67] A. Sivashanmugam, T.P. Kumar, N.G. Renganathan, S. Gopukumar, J. *Appl. Electrochem.* 34 (11) (2004) 1135–1139.
- [68] R. Udhayan, N. Muniyandi, P.B. Mathur, *Br. Corros. J.* 27 (1) (1992) 68–71.
- [69] L. Wang, S.S. Welborn, H. Kumar, M.N. Li, Z.Y. Wang, V.B. Shenoy, E. Detsi, *Adv. Energy Mater.* (2019).
- [70] M.N. Obrovac, V.L. Chevrier, *Chem. Rev.* 114 (23) (2014) 11444–11502.
- [71] J. Niu, H. Gao, W. Ma, F. Luo, K. Yin, Z. Peng, Z. Zhang, *Energy Storage Mater.* 14 (2018) 351–360.
- [72] J. Niu, K. Yin, H. Gao, M. Song, W. Ma, Z. Peng, Z. Zhang, *Nanoscale* 11 (32) (2019) 15279–15288.
- [73] M. Song, J. Niu, K. Yin, H. Gao, C. Zhang, W. Ma, F. Luo, Z. Peng, Z. Zhang, *Nano Res.* 12 (4) (2019) 801–808.
- [74] M. Song, T. Zhang, J. Niu, H. Gao, Y. Shi, Y. Zhang, W. Ma, Z. Zhang, *J. Power Sources* 451 (2020) 227735.
- [75] L.M. Watson, C.A.W. Marshall, C.P. Cardoso, *J. Phys. F Met. Phys.* 14 (1) (1984) 113–121.
- [76] F. Murgia, D. Laurencin, E.T. Weldekidan, L. Stievano, L. Monconduit, M.L. Doublet, R. Berthelot, *Electrochim. Acta* 259 (2018) 276–283.
- [77] Y. Cheng, Y. Shao, L.R. Parent, M.L. Sushko, G. Li, P.V. Sushko, N.D. Browning, C. Wang, J. Liu, *Adv. Mater.* 27 (42) (2015) 6598–6605.
- [78] F. Murgia, L. Monconduit, L. Stievano, R. Berthelot, *Electrochim. Acta* 209 (2016) 730–736.
- [79] L. Blondeau, E. Foy, H. Khodja, M. Gauthier, *J. Phys. Chem. C* 123 (2) (2019) 1120–1126.
- [80] A. Kitada, Y. Kang, Y. Uchimoto, K. Murase, *ECS Trans.* 58 (36) (2014) 75–80.
- [81] Y. Maeda, P. Touzain, *Electrochim. Acta* 33 (11) (1988) 1493–1497.
- [82] Y. Maeda, P. Touzain, L. Bonnetain, *Synth. Met.* 24 (3) (1988) 267–270.
- [83] D.-M. Kim, S.C. Jung, S. Ha, Y. Kim, Y. Park, J.H. Ryu, Y.-K. Han, K.T. Lee, *Chem. Mater.* 30 (10) (2018) 3199–3203.
- [84] D. Er, E. Detsi, H. Kumar, V.B. Shenoy, *ACS Energy Lett.* 1 (3) (2016) 638–645.
- [85] H.D. Lim, D.H. Kim, S. Park, M.E. Lee, H.J. Jin, S. Yu, S.H. Oh, Y.S. Yun, *Acs Appl. Mater. Interfaces* 11 (42) (2019) 38754–38761.
- [86] P. Novák, R. Imhof, O. Haas, *Electrochim. Acta* 45 (1-2) (1999) 351–367.
- [87] C. Chen, J. Wang, Q. Zhao, Y. Wang, J. Chen, *ACS Energy Lett.* (2016) 1165–1172.
- [88] N. Wu, Y.-C. Lyu, R.-J. Xiao, X. Yu, Y.-X. Yin, X.-Q. Yang, H. Li, L. Gu, Y.-G. Guo, *NPG Asia Mater.* 6 (8) (2014) e120.
- [89] N. Wu, Z.-Z. Yang, H.-R. Yao, Y.-X. Yin, L. Gu, Y.-G. Guo, *Angew. Chem. Int. Ed.* 54 (19) (2015) 5757–5761.
- [90] J. Zeng, Y. Yang, C. Li, J.Q. Li, J.X. Huang, J. Wang, J.B. Zhao, *Electrochim. Acta* 247 (2017) 265–270.
- [91] S. Banerjee, S.K. Pati, *Chem. Commun.* 52 (54) (2016) 8381–8384.